Design of an Aviation Dual-Three-Phase High-Power High-Speed Permanent Magnet Assisted Synchronous Reluctance Starter-Generator With Antishort-Circuit Ability

Hong Guo, *Senior Member, IEEE*, Xu He, Jinquan Xu, *Senior Member, IEEE*, Wei Tian, Gaoyang Sun, Laicai Ju, and Dehong Li

***Abstract*—This article proposes a novel dual-three-phase high-power high-speed permanent magnet assisted synchronous reluctance starter generator (PMaSynR SG) for aviation application, which has the characteristics of high efficiency, high power density, high reliability, and excellent antishort-circuit ability. The proposed PMaSynR SG can obtain higher efficiency and power density by embedding permanent magnet in the rotor topology compared with the synchronous reluctance generator, and has better antishort-circuit ability compared with the permanent magnet synchronous starter-generator. Moreover, design of dual-three-phase winding is adopted, which not only reduces the phase current, but also improves the reliability. In this article, the topological structure, characteristics and principle of PMaSynR SG are systematically studied at first. Second, a simplified *dq*-axis equivalent magnetic circuit model is established, and the expressions of *dq*-axis inductance and permanent magnet flux linkage are derived on the basis of the basic parameter selection. Then, combined with parameter sensitivity analysis, the influence law of rotor structural parameters on antishort-circuit ability and electromagnetic performance is revealed. Finally, a 40 kW 24 000 r/min PMaSynR SG is designed and manufactured. The simulation and experimental results show that the proposed PMaSynR SG has excellent electromagnetic performance with the power density of 3.1 kW/kg and the efficiency of 94%, while the short-circuit current is only 59% of its rated value.**

***Index Terms*—Antishort-circuit ability, dual-three-phase motor, permanent magnet assisted synchronous reluctance motor, starter generator.**

Manuscript received October 14, 2021; revised January 25, 2022 and March 19, 2022; accepted April 29, 2022. Date of publication May 3, 2022; date of current version June 24, 2022. This work was supported in part by the National Natural Science Foundation of China under Grant 52177028, in part by the Aeronautical Science Foundation of China under Grant 201907051002, and in part by Major Program of the National Natural Science Foundation of China under Grant 51890882. Recommended for publication by Associate Editor L. V. Iyer. *(Corresponding author: Jinquan Xu.)*

Hong Guo and Jinquan Xu are with the School of Automation Science and Electrical Engineering, Science and Technology on Aircraft Control Laboratory, Beihang University, Beijing 100191, China, and also with the Ningbo Innovation Research Institute, Ningbo 315615, China (e-mail: guohong_buaa@163.com; xujinquan@buaa.edu.cn).

Xu He and Gaoyang Sun are with the School of Automation Science and Electrical Engineering, Science and Technology on Aircraft Control Laboratory, Beihang University, Beijing 100191, China (e-mail: hexuzl@buaa.edu.cn; gy_sun@buaa.edu.cn).

Wei Tian is with the School of Electrical and Information Engineering, Jiangsu University, Zhenjiang 212013, China (e-mail: tw430725@163.com).

Laicai Ju is with the Beijing Shuguang Aviation Electric Co., Ltd., Beijing 100028, China (e-mail: julaicai123@163.com).

Dehong Li is with the Aviation Industry Helicopter Design and Research Institute, Tianjin 300480, China (e-mail: lidehong602@163.com).

Color versions of one or more figures in this article are available at https://doi.org/10.1109/TPEL.2022.3172339.

Digital Object Identifier 10.1109/TPEL.2022.3172339

I. Introduction

DUE to the high integration, high power density, and good maintainability, the starter-generator system has been considered a key technology for the more-electric/all-electric aircraft, which can operate as the motor to start the aero-engine and operate as the generator to supply the electrical power for the airborne equipment [1]–[3]. With the increasing electrification of airborne equipment, the electrical power capacity of the starter-generator system has increased sharply. Therefore, the high-power high-speed starter-generator system has attracted much attention for the modern aircraft power system in recent years [4]–[6].

In the past, considerable efforts in this field have been made, which can be mainly classified into three categories: three-stage brushless synchronous generator (TBSG), switched reluctance starter-generator (SRSG), and permanent magnet synchronous starter-generator (PMSSG) [7]–[9]. The TBSG has the advantages of high power, simple control structure, and high technical maturity, which has been widely applied as the main electrical power system of modern aircraft, such as A380 and COMAC C919 [10], [11]. However, due to the complex structure of the brushless excitation rotor, it is difficult to achieve the high-speed operation and high power density. The SRSG has the simple rotor structure without excitation winding or permanent magnet, which is suitable for the high-speed and high temperature operation [12], [13]. It has been successfully applied for the fighter F-35. However, the SRSG suffers from the issues of low efficiency, high torque fluctuation, and low power density. In contrast, the PMSSG has the excellent properties in power density, efficiency, and electromagnetic performance, which make it a potential candidate in the starter-generator applications [14]–[16]. However, the PMSSG has not been applied to manned aircraft power supply system due to the difficulty of permanent magnet demagnetization and the risk of short circuit.

The permanent magnet assisted synchronous reluctance starter-generator (PMaSynR SG) is characterized by a high-speed synchronous reluctance rotor topology by embedding permanent magnet, which has the merits of high power density, high efficiency [17]–[20]. Meanwhile, the antishort-circuit of PMaSynR SG is improved by reducing the usage of permanent magnet. Therefore, PMaSynR SG has attracted much attention in recent years. In [21]–[23], a PMaSynR motor design method is proposed to improve the output torque performance and reduce torque ripple by changing the rotor topology. In [24], the optimization design approach considering the magnetic saliency and PM usage is proposed for the PMaSynR motor. In [25], the analytical model of the PMaSynR motor is proposed to reveal the relationship between the PM thickness and the demagnetization. In [26], a five-phase PMaSynR motor is proposed to improve the reliability by considering the effects of irreversible demagnetization and mechanical deformation. In [27], a triple-redundant three-phase PMaSynR motor is proposed to guarantee the uninterrupted operation performance in fault condition. In addition, the fault tolerance performance of the proposed three-redundant PMaSynR motor is evaluated in [28] and [29]. In [30] and [31], the fault tolerant performance comparison for the dual three-phase synchronous reluctance motor on half control mode is proposed considering two different winding configurations. To solve for the short-circuit current issue, considerable efforts have been conducted for the aviation starter-generator system. The traditional three-stage brushless synchronous generator can completely eliminate the short-circuit current by cancelling the excitation current [32], [33]. In [34]–[37], the permanent magnet machine with fractional-slot single-layer winding structure is proposed to reduce the short-circuit current by unit phase inductance. In [38], the antishort-circuit optimization design of the slot parameters is proposed for the permanent magnet machine in aerospace application. However, the antishort-circuit design by the unit phase inductance will result in the low power factor of the starter-generator system. Note that due to the existence of permanent magnet, the PMaSynR machine still suffers from the risk of the short-circuit fault. However, there is little literature concerning about the relationship between output performance and antishort-circuit design in the PMaSynR machine. Traditional PMaSynR machine design mostly concerns about the salient pole ratio, torque ripple. As for the aerospace starter generator, antishort-circuit ability is essential. The design of the PMaSynR SG with the tradeoff of the electromagnetic performance and antishort-circuit ability is interesting to discuss.

On the premise of ensuring reliability and antishort circuit performance, whether it is possible to employ the new electrical machine type as the aviation starter generator to improve the power density, the efficiency is worth studying. Motivated by this, a novel dual-three-phase PMaSynR SG is proposed for aviation, which has the excellent antishort-circuit ability, high power density, high efficiency, and high reliability, which is the first time to be proposed in aerospace application. The main contributions of this article are three aspects. First, the topology and characteristics of PMaSynR SG and the principle of PMaSynR SG system are discussed. The basic PMaSynR SG parameters selection is given, the simplified *dq*-axis magnetic circuit model is established, and the *dq*-axis inductance and permanent magnetic flux linkage are derived. Second, the influence of the rotor structural parameters on the antishort-circuit ability and electromagnetic characteristics is revealed by sensitivity analysis of magnetic barriers, magnetic bridges, and permanent magnet. With the tradeoff of the high electromagnetic performance and excellent antishort-circuit ability, the design range of rotor parameters is given. Finally, a 40 kW 24 000 r/min PMaSynR SG is designed and manufactured. Simulation and experimental results show that the proposed PMaSynR SG has excellent electromagnetic performance, with the power density of 3.1 kW/kg and the efficiency of 94%, while the short-circuit current is only 59% of its rated value and the feasibility of the PMaSynR SG applied in aerospace starter generator power system is verified.

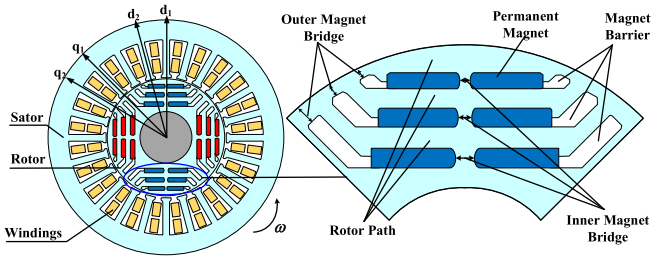

Fig. 1. Proposed PMaSynR SG scheme.

II. PMASYNR SG Topologies and Features

To satisfy the requirements of high speed, high power density, high efficiency, and high reliability for modern aircraft, a novel dual-three-phase PMaSynR SG is proposed in this article, as shown in Fig. 1.

The stator winding adopts a dual-three-phase structure with 30° phase-shifted, which effectively reduces the phase current. The rotor adopts a three-layer magnetic barrier structure with embedding permanent magnet to obtain a high proportion of reluctance torque and a low proportion of permanent magnet torque, which achieves high power density and high efficiency. Meanwhile, the mathematical model of the dual-three-phase PMaSynR SG is adopted. The north direction of permanent magnet is defined as the d_1-axis (short to *d*-axis) positive direction, and the q_1-axis (short to *q*-axis), is located electrical 90° counterclockwise to the d_1-axis while, d_2-axis and q_2-axis are located electrical angle of 30° counterclockwise to d_1-axis and q_1-axis, respectively.

Note that the output characteristics and antishort-circuit ability are affected by the design of the permanent magnet flux linkage and the *dq*-axis inductance. However, the antishort-circuit ability and output characteristics are mutually restricted and contradictory. Therefore, how to design a PMaSynR SG with both excellent output characteristics and antishort-circuit ability is the research focus in this article, which is described in details later.

A. Mathematical Model of PMaSynR SG System

The proposed PMaSynR SG system is mainly consist of the PMaSynR SG and the power converter. Based on the PMaSynR SG system principle and the dual three-phase machine characteristics, the mathematical model of the dual three-phase PMaSynR SG is established. The dual *d-q* coordinates transformation is adopted to convert $A_1B_1C_1$-$A_2B_2C_2$ into $d_1q_1o_1$-$d_2q_2o_2$. In addition, internal resistance of the high-speed PMaSynR SG is ignored in the analysis because it is far less than inductive reactance.

Assuming that the magnetic circuit of PMaSynR SG is linear, ignoring magnetic saturation and hysteresis loss, the steady-state voltage (1), and inductance matrix $\boldsymbol{L_{dq0}}$ (2) are as follows:

$$\begin{bmatrix} u_{d1} \\ u_{q1} \\ u_{d2} \\ u_{q2} \end{bmatrix} = \begin{bmatrix} 0 & -\omega & 0 & 0 \\ \omega & 0 & 0 & 0 \\ 0 & 0 & 0 & -\omega \\ 0 & 0 & \omega & 0 \end{bmatrix} \left(\boldsymbol{L_{dq0}} \begin{bmatrix} i_{d1} \\ i_{q1} \\ i_{d2} \\ i_{q2} \end{bmatrix} + \psi_{pm} \begin{bmatrix} 1 \\ 0 \\ 1 \\ 0 \end{bmatrix} \right) \tag{1}$$

where u_{d1}, u_{q1}, u_{d2}, u_{q2} are the dual *dq*-axis voltage, i_{d1}, i_{q1}, i_{d2}, i_{q2} are the dual *dq*-axis current, ψ_{pm} is the permanent magnet flux linkage, and $\boldsymbol{L_{dq0}}$ (2) shown at the bottom of this page, is the inductance matrix. Due to the influence of the complex rotor magnetic circuit saturation, the *dq*-axis inductance is not only related to the rotor structure parameters, but also closely related to the current. Therefore, the dual *dq*-axis inductance can be expressed as L_{d1} (i_{d1}, i_{q1}, i_{d2}, i_{q2}), L_{q1} (i_{d1}, i_{q1}, i_{d2}, i_{q2}), L_{d2} (i_{d1}, i_{q1}, i_{d2}, i_{q2}), L_{q2} (i_{d1}, i_{q1}, i_{d2}, i_{q2}), the dual *dq*-axis main inductance can be expressed as L_{dd} (i_{d1}, i_{q1}, i_{d2}, i_{q2}), L_{qq} (i_{d1}, i_{q1}, i_{d2}, i_{q2}), dual *dq*-axis main self-induction can be expressed as L_{aad}(i_{d1}, i_{q1}, i_{d2}, i_{q2}), L_{aaq} (i_{d1}, i_{q1}, i_{d2}, i_{q2}), and leakage inductance is l_{aal} (i_{d1}, i_{q1}, i_{d2}, i_{q2}). The abovementioned expressions are abbreviated as L_{d1}, L_{q1}, L_{d2}, L_{q2}, L_{dd}, L_{qq}, L_{aad}, L_{aaq}, l_{aal}. Among them, $L_{d1} = L_{d2} = L_{dd} + l_{aal}$, $L_{q1} = L_{q2} = L_{qq} + l_{aal}$, $L_{dd} = 1.5L_{aad}$, $L_{qq} = 1.5L_{aaq}$

The flux linkage equation is

$$\begin{bmatrix} \psi_{d1} \\ \psi_{q1} \\ \psi_{d2} \\ \psi_{q2} \end{bmatrix} = \boldsymbol{L_{dq0}} \begin{bmatrix} i_{d1} \\ i_{q1} \\ i_{d2} \\ i_{q2} \end{bmatrix} + \psi_{pm} \begin{bmatrix} 1 \\ 0 \\ 1 \\ 0 \end{bmatrix} \tag{3}$$

where ψ_{d1}, ψ_{d2}, are *d*-axis flux linkage generated by first and second set of three phase winding current and permanent magnet, ψ_{q1}, ψ_{q2} are *q*-axis flux linkage generated by first and second set of three phase winding current.

The electromagnetic torque equation is

$$T_e = \frac{3}{2} n_p \left[(i_{q1}\psi_{d1} - i_{d1}\psi_{q1}) + (i_{q2}\psi_{d2} - i_{d2}\psi_{q2}) \right]$$

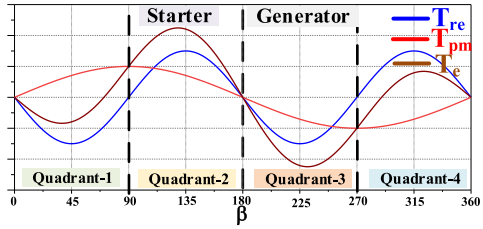

Fig. 2. PMaSynR SG torque characteristics curve.

$$= \frac{3}{2} n_p \left[\psi_{pm} (i_{q1} + i_{q2}) + (L_{d1} - L_{q1}) (i_{d1} i_{q1} + i_{d2} i_{q2}) \right] \tag{4}$$

where n_p is the pole pairs.

Generally, for proper of control, $i_d = i_{d1} = i_{d2}$, $i_q = i_{q1} = i_{q2}$, (4) can be written as

$$\begin{aligned} T_e &= \frac{3}{2} n_p \left[2\psi_{pm} i_q + 2 (L_{d1} - L_{q1}) i_d i_q \right] \\ &= 3n_p \left[\psi_{pm} i_q + (L_{d1} - L_{q1}) i_d i_q \right] = T_{re} + T_{pm} \end{aligned} \tag{5}$$

where T_{re} is reluctance torque and T_{pm} is permanent magnet torque.

Ratio of permanent magnet torque to electromagnetic torque λ can be obtained as

$$\lambda = fracT_{pm}T_e \ = \frac{\psi_{pm}}{\psi_{pm} + (L_{d1} - L_{q1}) i_d}. \tag{6}$$

Torque characteristics of PMaSynR SG can be described as Fig. 2, where β is the current angle with respect to the positive direction of *d*-axis. The maximum electromagnetic torque of the starting process and power generation can be obtained only when the current is in the second quadrant and third quadrant, respectively.

Meanwhile, in order to intuitively compare the difference of *d-q* inductance and describe the salient pole performance, the salient pole ratio ρ is introduced as (7). ρ is a crucial parameter affecting the power factor cosφ, where φ is the angle between voltage u_s and current i_s, and u_s is vector synthesis of u_{d1}, u_{d2}, u_{q1}, and u_{q2}

$$\rho \ = \frac{L_{q1}}{L_{d1}}. \tag{7}$$

The output characteristic of the PMaSynR SG will be significantly improved if increasing the difference of *dq*-axis inductance L_{d1}-L_{q1} and permanent magnet flux linkage. However, if short-circuit fault occurs during the power generation, SG will generate short circuit current. The more the usage permanent magnet is, the higher the short circuit current is, which may damage the PMaSynR SG or even the PMaSynR SG system.

$$\boldsymbol{L_{dq0}} = \begin{bmatrix} L_{d1}(i_{d1}, i_{q1}, i_{d2}, i_{q2}) & 0 & L_{dd}(i_{d1}, i_{q1}, i_{d2}, i_{q2}) & 0 \\ 0 & L_{q1}(i_{d1}, i_{q1}, i_{d2}, i_{q2}) & 0 & L_{qq}(i_{d1}, i_{q1}, i_{d2}, i_{q2}) \\ L_{dd}(i_{d1}, i_{q1}, i_{d2}, i_{q2}) & 0 & L_{d2}(i_{d1}, i_{q1}, i_{d2}, i_{q2}) & 0 \\ 0 & L_{qq}(i_{d1}, i_{q1}, i_{d2}, i_{q2}) & 0 & L_{q2}(i_{d1}, i_{q1}, i_{d2}, i_{q2}) \end{bmatrix}. \tag{2}$$

In practical engineering, to avoid the fault propagation, when the short-circuit occurs in one set of three-phase winding, the other set of three-phase winding will be turned OFF for safety consideration. Here, we assume that the short-circuit fault happens in the second set of three-phase winding, while the first set of three-phase winding is turned OFF. That is, the terminal voltage of the second set of three phase $u_{\mathrm{d}2}$ and $u_{\mathrm{q}2}$ is 0, while the current of the first set of three phase $i_{\mathrm{d}1}$ and $i_{\mathrm{q}1}$ is 0, where the *d-q* voltage and current are $u_{\mathrm{dq}} = [u_{\mathrm{d}1}\ u_{\mathrm{q}1}\ 0\ 0]^{\mathrm{T}}$, $i_{\mathrm{dq}} = [0\ 0\ i_{\mathrm{d}2}\ i_{\mathrm{q}2}]^{\mathrm{T}}$. Substitute them into (1)

$$\begin{bmatrix} u_{d1} \\ u_{q1} \\ 0 \\ 0 \end{bmatrix} = \begin{bmatrix} 0 & -\omega & 0 & 0 \\ \omega & 0 & 0 & 0 \\ 0 & 0 & 0 & -\omega \\ 0 & 0 & \omega & 0 \end{bmatrix} \left(\boldsymbol{L_{dq}}_0 \begin{bmatrix} 0 \\ 0 \\ i_{d2} \\ i_{q2} \end{bmatrix} + \psi_{pm} \begin{bmatrix} 1 \\ 0 \\ 1 \\ 0 \end{bmatrix} \right). \tag{8}$$

Furthermore,

$$\begin{bmatrix} u_{d1} \\ u_{q1} \\ 0 \\ 0 \end{bmatrix} = \begin{bmatrix} -\omega(L_{qq} i_{q2}) \\ \omega\left(L_{dd} i_{d2} + \psi_{pm}\right) \\ -\omega\left(L_{q2} i_{q2}\right) \\ \omega\left(L_{d2} i_{d2} + \psi_{pm}\right) \end{bmatrix}$$

$$\rightarrow \begin{cases} u_{d1} = 0 \\ u_{q1} = \frac{\omega l_{aal} \psi_{pm}}{L_{dd} + l_{aal}} \\ i_{d2} = -\frac{\psi_{pm}}{L_{d2}} = -\frac{\psi_{pm}}{L_{dd} + l_{aal}} \\ i_{q2} = 0 \end{cases}. \tag{9}$$

In (9), $i_{\mathrm{d}2}$, i_{q2} represents the short-circuit current of the PMaSynR SG in single-three-phase short circuit fault condition, l_{aal} is leakage inductance. Since $i_{\mathrm{q}2} = 0$, the short circuit current of the second set of three phase windings is $-\frac{\psi_{pm}}{L_{dd}+l_{aal}}$. In addition, when the second set of three phase windings short-circuit fault occurs, due to the existence of leakage inductance, the first set of three-phase windings induces a little voltage $u_{\mathrm{q}1}$.

When dual-three-phase short circuit fault occurs, similarly, the dual-three phase power tubes are turned OFF, the terminal voltage of dual three phase windings is 0, where the voltage is $u_{\mathrm{dq}} = [0\ 0\ 0\ 0]^{\mathrm{T}}$. Substitute it into (1)

$$\begin{cases} i_{d1} = -\frac{\psi_{pm}}{L_{d1}+L_{dd}} = -\frac{\psi_{pm}}{2L_{dd}+l_{aal}} \\ i_{q1} = 0 \\ i_{d2} = -\frac{\psi_{pm}}{2L_{dd}+l_{aal}} \\ i_{q2} = 0. \end{cases} \tag{10}$$

Equation (10) represents the short-circuit current of the PMaSynR SG in dual three phase short circuit fault condition. In this condition, the terminal voltages of dual three phase windings are all zero. Each phase short-circuit current is $-\frac{\psi_{pm}}{2L_{dd}+l_{aal}}$. Note that the short-circuit current in dual-three-phase short-circuit fault condition is less than that in single-three-phase short-circuit fault condition.

Equations (11) and (12) represent the ratio of the short-circuit current to the rated current in single- and dual-three-phase short-circuit fault conditions, respectively, where k_{s1} and k_{s2} is the ratio of single-three-phase and dual-three-phase short-circuit current, respectively, to rated current

$$k_{s1} = \frac{\psi_{pm}}{\left(L_{dd} + l_{aal}\right) i_s} \tag{11}$$

TABLE I
PMASYNR SG PERFORMANCE REQUIREMENTS

Starting torque	20N•m
Starting speed at constant torque	0~6000rpm
Starting speed at constant power	6000~9000rpm
Rated power generation speed	24000rpm
Rated power generation power	40kW
Peak voltage ripple	⩽6V

$$k_{s2} = \frac{\psi_{pm}}{\left(2L_{dd} + l_{aal}\right) i_s}. \tag{12}$$

From (11) and (12), the variation trend of $k_{\mathrm{s}1}$ and $k_{\mathrm{s}2}$ is the same. They are both determined by the permanent magnet flux linkage and *d*-axis inductance, and $k_{\mathrm{s}1} > k_{\mathrm{s}2}$.

For the description of the antishort-circuit ability, k_s is defined as the ratio of the short-circuit current to the rated current. When k_{s}>1, the short-circuit current is higher than the rated current, which will cause the overheat issue for the PMaSynR SG in short-circuit fault condition. When $k_{\mathrm{s}} < 1$, the short-circuit current is lower than the rated current, which shows the excellent antishort-circuit performance of the PMaSynR SG.

Generally, the safety of PMaSynR SG can be guaranteed if the short-circuit current is less than the rated generation current. The antishort-circuit ability can be improved if reducing the permanent magnetic flux linkage or increasing the *d*-axis inductance. However, as mentioned previously, the output characteristics of PMaSynR SG can be improved if increasing the salient ratio or the usage of permanent magnet, which conflicts with the improvement of antishort-circuit ability. Therefore, the design of the inductance and the permanent magnet flux linkage are the core of PMaSynR SG design.

III. DESIGN OF PMASYNR SG WITH ANTISHORT-CIRCUIT ABILITY

The design of the PMASYNR SG with antishort-circuit ability in this section is consist of three aspects. First, the basic parameter selection of PMaSynR SG is given. Next, the rotor topological structure is studied, the *dq*-axis equivalent magnetic circuit model is established, and the expressions of *d-q* inductance and permanent magnet flux linkage are derived. Finally, the influence law of the rotor structure on output performance and antishort-circuit ability is revealed by the rotor structure parameter sensitivity analysis. It provides the basis and reference for the design of PMaSynR SG.

A. PMaSynR SG Basic Parameters Section

The design requirements of the high-speed, high-power PMaSynR SG in aviation are shown in Table I.

According to the requirements of Table I, air gap, pole pairs, winding structure, slot number, and materials of stator and rotor need be selected at first.

1) Air Gap Thickness: The electromagnetic torque of PMaSynR SG is mainly depended by the reluctance torque. The thickness of the air gap directly affects the *dq*-axis inductance

TABLE II
PMASYNR SG BASIC PARAMETERS

PARAMETERS	Value
Phase	Dual-three-phase
Stator outer diameter	121mm
Rotor outer diameter	61mm
Stack length	93mm
Air gap	0.5mm
Slot	24
Pole-pair	2
Stator sheet material	20JNEH1200
Rotor sheet material	35XH680T
PM material	SmCo32

and the reluctance torque. Generally, the air gap is set to 0.2–2 mm. Taking the consideration of manufacturing technique and good salient pole effect, the air gap is set as 0.5 mm.

2) Pole Pairs: Since PMaSynR SG rotates at 24 000 r/min during power generation, the mechanical frequency is 400 Hz. As for the high current power converter, the switch frequency is generally employed as about 20 kHz. Therefore, the pole pairs should not be more than three to guarantee control effect. Taking the consideration of switch frequency, control effect, and good salient pole effect, pole pairs is set as two, and the fundamental frequency is 800 Hz.

3) Winding Structure: Due to the requirements of 270 VDC, 40 kW power generation output, the winding structure of N∗3 phase is a good choice. This structure can reduce the level of phase current and avoid power tubes to be operated in parallel, which may cause uneven current flow. Meanwhile, N sets of three phase winding neutral points isolated from each other. The PMaSynR SG is characterized of flexible control strategy, which can be controlled as a N∗3 phase electrical machine or a multiphase electrical machine. Taking the consideration of phase current level, control effect, dual-three-phase winding structure with the phase shift of 30° is adopted.

4) Slot Number: With the selection of pole pairs and dual three phase winding structure determined, the number of slots with the balance the electromagnetic force of each phase and full-pitch winding structure should be a multiple of 12, i.e., 12, 24, 36... In addition, it should be as high as possible to reduce the torque ripple. Since low outer diameter of stator and rotor of high-speed machines, if the number of slots ≥ 36, the stator teeth are too thin to manufacture. Therefore, the slot number is set as 24.

5) Material of Stator, Rotor, and Permanent Magnet: Taking the consideration of reducing stator core loss and improving efficiency, the material of stator laminations is ultrathin silicon steel lamination 20JNEH1200. For fulfilling the requirements of high-speed rotor mechanical strength, the material of rotor laminations is 35XH680T with the maximum yield stress over 600 MPa. For design requirements of high power density, the material of permanent magnet is SmCo32 with high temperature resistance and high remanence.

The selection results of PMaSynR SG parameters are shown in Table II.

The topological structure of the rotor and the design of permanent magnet not only affect the electromagnetic output characteristics, but also affect antishort-circuit ability. However, there are many parameters in rotor topological structure, and the relationship between the output performance and antishort-circuit ability of the PMaSynR SG needs further analysis.

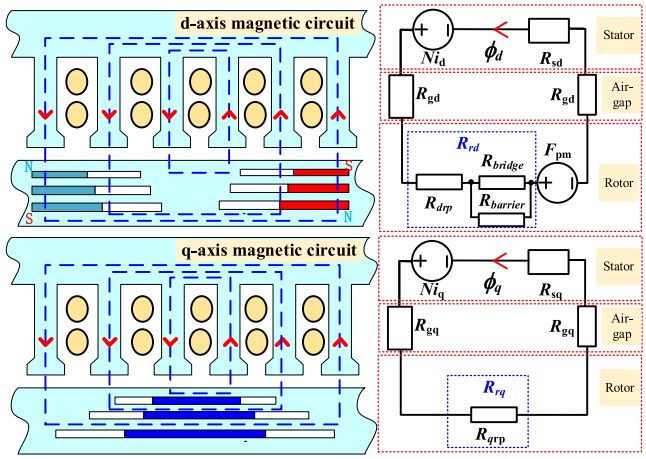

Fig. 3. *Dq*-axis magnetic circuit model and simplified equivalent model.

B. Analysis and Derivation of dq-Axis Inductance

Dq-axis inductance includes the main inductance and leakage inductance. Leakage inductance does not participate in the energy conversion and is low, which is ignored temporarily in the analysis. Only the main inductance is considered. *Dq*-axis magnetic circuit model and simplified equivalent model of one set of windings are established, respectively, as shown in Fig. 3.

In Fig. 4, N_{id} and N_{iq} are the magnetomotive force generated by the *dq*-axis current, R_{sd} and R_{sq} are the stator *dq*-axis reluctance, R_{gd} and R_{gq} are the air-gap *dq*-axis reluctance, R_{rd} and R_{rq} are the rotor *dq*-axis equivalent reluctance, R_{drp} and R_{qrp} are the rotor *dq*-axis rotor path reluctance, R_{bridge} is the magnetic bridge reluctance, R_{barrier} is magnetic barrier reluctance, which is consist of permanent magnet reluctance and residual air magnetic barrier reluctance. Since the relative permeability of permanent magnet is close to that of air, the relative permeability of R_{barrier} is regarded as 1. F_{pm} is the total magnetomotive force generated by the three layers of permanent magnet φ_{d} and φ_{q} are the *dq*-axis magnetic flux.

From Fig. 3, *dq*-axis magnetomotive force $\mathrm{F_d}$, $\mathrm{F_q}$ and R_{rd}, R_{rq} can be obtained

$$F_d = Ni_d - F_{pm} = \phi_d \ (R_{\mathrm{sd}} + 2R_{\mathrm{gd}} + R_{\mathrm{rd}}) \tag{13}$$

$$F_q = N\, i_q = \phi_q \ (R_{\mathrm{sq}} + 2R_{\mathrm{gq}} + R_{\mathrm{rq}}) \tag{14}$$

$$R_{\mathrm{rd}} = R_{\mathrm{drp}} + R_{\mathrm{bridge}} // R_{\mathrm{barrier}} \tag{15}$$

$$R_{\mathrm{rq}} = R_{\mathrm{qrp}}. \tag{16}$$

Then, the *dq*-axis main self-inductance L_{aad}, L_{aaq}, the *dq*-axis main inductance L_{dd}, L_{qq}, and salient pole ratio ρ can be

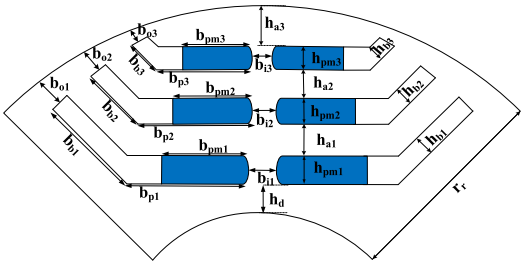

Fig. 4. Rotor structure model.

calculated

$$L_{aad} = \frac{N^2\phi_d}{F_d} = \frac{N^2}{2R_{gd} + R_{\mathrm{sd}} + R_{rd}} \tag{17}$$

$$L_{aaq} = \frac{N^2\phi_q}{F_q} = \frac{N^2}{2R_{gq} + R_{sq} + R_{rq}} \tag{18}$$

$$L_{dd} = 1.5\, L_{aad} = \frac{1.5N^2}{2R_{gd} + R_{\mathrm{sd}} + R_{rd}} \tag{19}$$

$$L_{qq} = 1.5\, L_{aaq} = \frac{1.5N^2}{2R_{gq} + R_{sq} + R_{rq}} \tag{20}$$

$$\rho = \frac{L_{q1}}{L_{d1}} = \frac{L_{qq} + l_{aal}}{L_{dd} + l_{aal}} = \frac{2R_{\mathrm{gd}} + R_{rd} + \frac{2l_{aal}}{3N^2}}{2R_{gq} + R_{rq} + \frac{2l_{aal}}{3N^2}} \tag{21}$$

where N is effective number of turns with the consideration of the winding factor.

Since dq-axis air gap reluctance is common to air gap, it can be considered that $R_{\mathrm{gd}} = R_{\mathrm{gq}}$. Therefore, it can be seen that salient pole effect is mainly determined by the difference between R_{rd} and R_{rq}.

In order to obtain the reluctance of each rotor position, the rotor structure model is established, as shown in Fig. 4. In Fig. 4, b_{o1}, b_{o2}, b_{o3} are the width of outer magnetic bridge, $\mathrm{b_{i1}}$, $\mathrm{b_{i2}}$, $\mathrm{b_{i3}}$ are the width of inner magnetic bridge, b_{b1}, b_{b2}, b_{b3} are the width of inclined air magnetic barrier, and the value is also equal to the thickness of outer magnetic bridge, b_{p1}, b_{p2}, b_{p3} are the width of horizontal air magnetic barrier, b_{pm1}, b_{pm2}, b_{pm3} are the width of permanent magnet, $h_{\mathrm{b1}}, h_{\mathrm{b2}}, h_{\mathrm{b3}}$ are the thickness of horizontal air magnetic barrier, and the value is also equal to the thickness of permanent magnet and inner magnetic bridge, h_{a1}, h_{a2} are the thickness of rotor path, and the horizontal rotor path is set to be equal to the inclined rotor path, h_{a3} is the thickness between third layer of horizontal magnetic barrier and outer rotor diameter, h_{d} is the thickness between the first horizontal magnetic barrier and the inner diameter of the rotor, and r_{r} is the radial thickness of the rotor.

The reluctance of each part can be calculated

$$R = \frac{l}{\mu_0\mu_r A} = \frac{l}{\mu_0\mu_r b l_{ef}} \tag{22}$$

where l is the length of the flux through part, μ_0 is the vacuum permeability, μ_{r} is the relative permeability, A is the area of the flux through part, l_{ef} is the axial length of the SG, and b is the radial length.

Note that the reluctance computation is an approximation in this article. All reluctances of the rotor are considered as a unique reluctance. Actually, they create a different magnetic potential in the rotor. $R_{\mathrm{bridge}}, R_{\mathrm{barrier}}, R_{\mathrm{drp}}, R_{\mathrm{qrp}}, R_{\mathrm{rq}}, R_{\mathrm{rd}}$ can be calculated as

$$\begin{aligned} R_{\mathrm{bridge}} &= R_{ob} + R_{ib} \\ &= \frac{1}{2\mu_0\mu_s l_{ef}}\left(\sum_{i=1}^{3}\frac{h_{bi}}{b_{oi}}\right) + \frac{1}{\mu_0\mu_s l_{ef}}\left(\sum_{i=1}^{3}\frac{h_{pmi}}{b_{ii}}\right) \\ &= \frac{1}{2\mu_0\mu_s l_{ef}}\left(\sum_{i=1}^{3}\frac{h_{bi}}{b_{oi}}\right) + 2\left(\sum_{i=1}^{3}\frac{h_{pmi}}{b_{ii}}\right) \end{aligned} \tag{23}$$

$$\begin{aligned} R_{\mathrm{barrier}} &= \mathrm{R}_{bh}\ //\mathrm{R}_{bi} \\ &= \frac{1}{2\mu_0 l_{ef}}\left(\sum_{i=1}^{3}\frac{h_{pmi}}{b_{pi}}\right) // \frac{1}{2\mu_0 l_{ef}}\left(\sum_{i=1}^{3}\frac{h_{bi}}{b_{bi}}\right) \\ &= \frac{1}{2\mu_0 l_{ef}}\left(\left(\sum_{i=1}^{3}\frac{h_{pmi}}{b_{pi}}\right) // \left(\sum_{i=1}^{3}\frac{h_{bi}}{b_{bi}}\right)\right) \end{aligned} \tag{24}$$

$$R_{drp} = \frac{1}{\mu_0\mu_n l_{ef}}\left(\sum_{i=1}^{3}\frac{h_{ai}}{2(b_{pi} + b_{bi} + b_{oi}) + b_{ii}}\right) \tag{25}$$

$$R_{\mathrm{rq}} = R_{qrp} = \frac{1}{\mu_0\mu_n l_{ef}}\ (R_{qrib1}//R_{qrib2}//R_{qrib3}) \tag{26}$$

where // is parallel symbol, which means multireluctances are in parallel, R_{ob} and R_{ib} are outer and inner magnetic bridge reluctance, respectively, μ_{s} and μ_{n} are the relative permeability of magnetic bridge at magnetic saturation, and the relative permeability of rotor path, respectively. R_{qrpi} is the rotor path reluctance in different layer $R_{qrpi} = \frac{2(b_{pi}+b_{bi}+b_{oi})+b_{ii}}{h_{ai}}$ $i = 1, 2$. In spite of the shape of the third rotor path is slightly different from that of the first two rotor paths, it has little influence on the overall performance due to the relatively high permeability of the rotor and low rotor path reluctance. Therefore, R_{qrp3} can be approximately calculated according to the expression of R_{qrp1}. $R_{qrpi} = \frac{2(b_{pi}+b_{bi}+b_{oi})+b_{ii}}{h_{ai}}$, $i = 1, 2, 3$

And R_{gd} and R_{gq} can be calculated as

$$R_{gd} = R_{gq} = \frac{4\delta}{\pi\mu_0 l_{ef} r} \tag{28}$$

where r is the rotor radius and δ is the thickness of the air gap.

Then, L_{dd} and L_{qq} can be calculated

$$L_{dd} = \frac{1.5N^2}{\frac{8\delta}{\pi\mu_0 l_{ef} r} + R_{rd}} \tag{29}$$

$$R_{\mathrm{rd}} = \frac{1}{\mu_0 l_{ef}}\left(\left(\frac{1}{\mu_n}\sum_{i=1}^{3}\frac{h_{ai}}{2(b_{pi}+b_{bi}+b_{oi})+b_{ii}}\right) + \frac{1}{2\mu_s}\left(\left(\sum_{i=1}^{3}\frac{h_{bi}}{b_{oi}}\right) + 2\left(\sum_{i=1}^{3}\frac{h_{pmi}}{b_{ii}}\right)\right)\right) // \frac{1}{2}\left(\left(\sum_{i=1}^{3}\frac{h_{pmi}}{b_{pi}}\right) // \left(\sum_{i=1}^{3}\frac{h_{bi}}{b_{bi}}\right)\right) \tag{27}$$

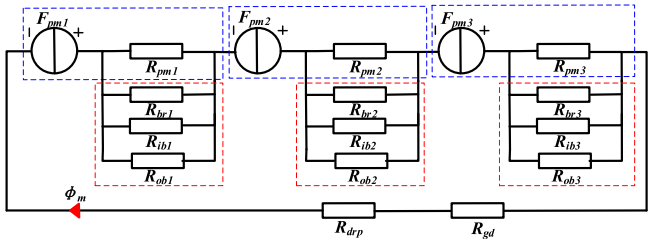

Fig. 5. Permanent magnet magnetic circuit model.

$$L_{qq} = \frac{1.5N^2\mu_0 l_{ef}}{\frac{8\delta}{\pi\mu_0 r} + \frac{1}{\mu_n}\left(R_{qrib1}//R_{qrib2}//R_{qrib3}\right)}. \tag{30}$$

C. Analysis and Derivation of Permanent Magnet Flux Linkage

Due to the existence of magnetic bridge and residual air magnetic barrier, flux leakage will pass through. In this article, only the flux leakage in the layer is considered and flux leakage between layers is ignored. Permanent magnet magnetic circuit model is established, as shown in Fig. 5.

In Fig. 5, the blue box is the equivalent model of permanent magnet, and the red box is the leakage reluctance, $F_{\rm pmi}$ is the magnetomotive generated by each layer of permanent magnet, ϕ_m is the main flux, $R_{\rm pmi}$ is the permanent magnet reluctance, and $R_{\rm bri}$ is the residual air magnetic barrier reluctance $i = 1$, 2, 3. In addition, the internal resistance of permanent magnet and magnetic leakage reluctance together constitute magnetic barrier reluctance and magnetic bridge reluctance. Since only the flux leakage at the located layer is considered, and the magnetic property of the permanent magnet is less affected by the external magnetic field, the magnetic field intensity H at each layer can be regarded as equal in the analysis process, then

$$\phi_m = \frac{F_{pm1} + F_{pm2} + F_{pm3}}{R_{gd} + R_{\rm barrier}//R_{\rm bridge} + R_{drp}}. \tag{31}$$

Permanent magnet flux linkage ϕ_{pmi} passing through the magnetic barrier and magnetic bridge of each layer is

$$\phi_{pmi} = \phi_m \ + \phi_{\sigma i} i = \ 1,\ 2,\ 3 \tag{32}$$

where $\phi_{\sigma i}$ is the magnetic flux leakage, including the outer magnetic bridge leakage $\phi_{\sigma oi}$, the inner magnetic bridge leakage $\phi_{\sigma ii}$, and the residual magnetic barrier ϕ_{pi}

$$\phi_{\sigma i} = \phi_{\sigma oi} \ + \phi_{\sigma ii} + \phi_{pi}. \tag{33}$$

The magnetic bridge is in saturation state, and the magnetic bridge saturation magnetic density is $B_{\rm s}$, then

$$\phi_{\sigma oi} = 2B_S b_{oi} l_{ef} \tag{34}$$

$$\phi_{\sigma ii} = B_S\ b_{ii} l_{ef}. \tag{35}$$

The magnetic vector potential drop of the magnetic bridge is equal to that of the residual air magnetic barrier. The residual air magnetic barrier reluctance is $R_{\rm r\text{-}barrier}$, which is consist of the horizontal magnetic barrier reluctance of no permanent magnet R_{nbhi} and the inclined magnetic barrier reluctance $R_{\rm bi}$, then

$$\phi_{pi} = \frac{B_S b_{ii} l_{ef} R_{ib}}{R_{r-\rm barrier}} = \frac{B_S b_{ii} l_{ef} R_{ib}}{R_{nbhi}//R_{bi}} \tag{36}$$

$$\mathrm{R}_{nbhi} = \frac{1}{2\mu_0 l_{ef}} \frac{h_{pmi}}{b_{pi} - b_{pmi}}. \tag{37}$$

Then, ϕ_{pmi} (38) shown at the bottom of next page and ψ_{pm} (39) shown at the bottom of next page can be obtained

Up to now, *dq*-axis inductance and permanent magnet flux linkage are deduced. From this, the expression of electromagnetic torque $T_{\rm e}$ (40) shown at the bottom of next page, the ratio of single-three-phase, dual-three-phase short-circuit current to rated current $k_{\rm s1}$ (41) shown at the bottom of next page, $k_{\rm s2}$ (42) shown at the bottom of next page can be calculated. In addition, the power factor $|\cos\varphi|$ at power generation state is also a consideration in the design, it can be expressed as

$$|\cos\varphi| = \left|\frac{P}{S}\right| \tag{43}$$

where P is active power and S is the apparent power

$$P = \Omega_m\ T_e \tag{44}$$

$$\begin{aligned} u_s &= \omega\sqrt{\left(u_{q1} + u_{q2}\right)^2 + \left(u_{d1} + u_{d2}\right)^2} \\ &= 2\omega\sqrt{\left(L_{d1} i_d + \psi_{pm}\right)^2 + \left(L_{q1} i_q\right)^2} \end{aligned} \tag{45}$$

where Ω_m is mechanical speed $\omega = n_p\ \Omega_m$

$$\begin{aligned} |\cos\varphi| \ &= \frac{\left[\psi_{pm} i_q + \left(L_{d1} - L_{q1}\right) i_d i_q\right]}{\sqrt{i_d^2 + i_q^2}\sqrt{\left(L_{d1} i_d + \psi_{pm}\right)^2 + \left(L_{q1} i_q\right)^2}} \\ &= \frac{(\rho - 1)\sin\beta cos\ \beta - \frac{\psi_{pm}}{L_{d1} i_s}\sin\beta}{\sqrt{\left(\cos\beta + \frac{\psi_{pm}}{L_{d1} i_s}\right)^2 + \rho^2 \sin^2\beta}}. \end{aligned} \tag{46}$$

For the consideration of the reliability of aviation PMaSynR SG, $|\frac{\psi_{pm}}{i_s L_{d1}}|$ needs to be less than 1. And furtherly, the relationship between rotor parameters and power factor can be obtained.

It can be seen that the relationship is complex and the high coupling. In order to further intuitively analyze the influence of different rotor parameters on output performance and antishort-circuit ability, sensitivity analysis of rotor structure parameters will be introduced as follows.

D. Rotor Structure Parameters Sensitivity Analysis on Output Performance and Antishort-Circuit Ability

The influence of rotor structure parameters, such as the size of the magnetic barrier, the magnetic bridge, and the permanent magnet on the output performance, power factor, and antishort-circuit ability is analyzed by analytical method and the mechanical strength is calculated by finite element (FE) method in this part. During the analysis, maximum torque per ampere (MTPA) control strategy under nonweakening magnetic state is adopted. According to Lagrange extremum theorem, auxiliary

functions are introduced

$$\mathrm{H}\left(i_{d1}, i_{q1}, \lambda_{dq}\right) = \sqrt{i_{d1}^2 + i_{q1}^2} + \lambda_{dq}\left\{T_e - 3n_p\left[\psi_{pm} i_q + \left(L_{d1} - L_{q1}\right) i_d i_q\right]\right\} \tag{47}$$

where λ_{dq} is Lagrangian. Take the partial derivatives of (48), and calculate the extremum of the electromagnetic torque. Then, i_{d}, i_{q} can be calculated

$$i_d = \frac{-\psi_{pm} + \sqrt{\psi_{pm}^2 + 8\left(L_{d1} - L_{q1}\right)^2 i_s^2}}{4\left(L_{d1} - L_{q1}\right)} \tag{48}$$

$$i_q = -\sqrt{i_s^2 - i_d^2}\,. \tag{49}$$

Substitute (48), (49) into (5), the relationship between T_{e} and i_{s} under MTPA can be obtained.

Short circuit current and rated current can be calculated and the ratio of short circuit current to rated current k_{sc} can be obtained. Since the short circuit current of dual-three-phase and that of single-three-phase changes in the same trend, only the single-three-phase short-circuit current is analyzed. Meanwhile, the difference of *dq*-axis inductance L_{d1}-L_{q1}, $|\cos\varphi|$, ρ are crucial factors affecting the electromagnetic performance and analyzed as well.

1) Comparison Between Analytical Model and FE Model: First of all, the accuracy of analytical model of *dq*-axis inductance and permanent magnet flux is discussed. Here, flux density is a sensitive parameter to compute the network, which is mainly depended on the relative permeability of magnetic bridge at magnetic saturation μ_{s} and the relative permeability of rotor path μ_{n}. In the process of computing the network, the rotor path is designed in the unsaturated region, and the rotor outer and inner magnetic bridge is designed in the saturated region due to the narrow bridge thickness.

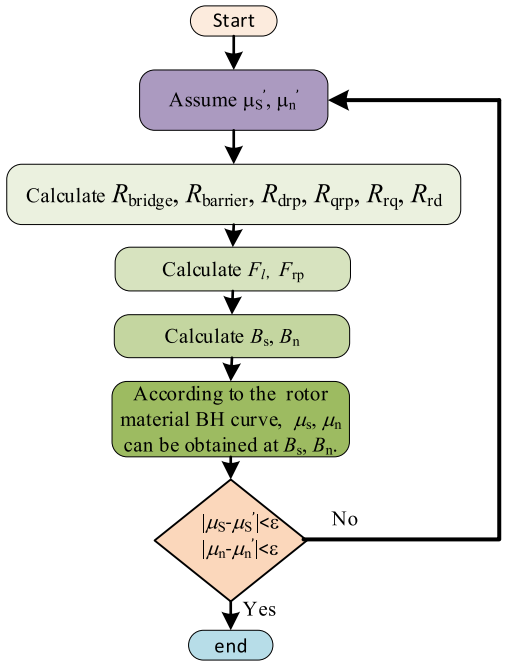

Fig. 6. Calculation process of μ_{s} and μ_{n}.

The calculation process of μ_{s} and μ_{n} can be described as Fig. 6.

Assume μ_{s}', μ_{n}', then calculate R_{bridge}, R_{barrier}, R_{drp}, R_{qrp}, R_{rq}, R_{rd}. According to the relationship between magnetomotive force and reluctance in Fig. 5, the barrier magnetomotive force

$$\phi_{pmi} = \frac{F_{pm1} + F_{pm2} + F_{pm3}}{R_{gd} + R_{\mathrm{barrier}}//R_{\mathrm{bridge}} + R_{drib}} + 2B_S b_{oi} l_{ef} + B_S b_{ii} l_{ef} + \frac{B_S b_{ii} l_{ef} R_{ib}}{R_{nbhi}//R_{bi}} \tag{38}$$

$$\psi_{pm} = N\phi_{pm} = N\left(\frac{F_{pm1} + F_{pm2} + F_{pm3}}{R_{gd} + R_{\mathrm{barrier}}//R_{\mathrm{bridge}} + R_{drib}} + 2B_S b_{oi} l_{ef} + B_S b_{ii} l_{ef} + \frac{B_S b_{ii} l_{ef} R_{ib}}{R_{nbhi}//R_{bi}}\right) \tag{39}$$

$$\begin{aligned} T_e &= 3p_n\left(L_{d1} - L_{q1}\right) i_s^2 \sin 2\beta + 3p_n \psi_{\mathrm{pm}} i_s \sin\beta = 3p_n\left(L_{dd} - L_{qq}\right) i_s^2 \sin 2\beta + 3p_n \psi_{\mathrm{pm}} i_s \sin\beta \\ &= 3p_n\left(\frac{1.5N^2}{\frac{8\delta}{\pi\mu_0 l_{ef} r} + R_{rd}} - \frac{1.5N^2\mu_0 l_{ef}}{\frac{8\delta}{\pi\mu_0 r} + \frac{1}{\mu_n}\left(R_{qrib1}//R_{qrib2}//R_{qrib3}\right)}\right) i_s^2 \sin 2\beta + 3p_n N \\ &\quad \left(\frac{F_{pm1} + F_{pm2} + F_{pm3}}{R_{gd} + R_{\mathrm{barrier}}//R_{\mathrm{bridge}} + R_{drib}} + 2B_S b_{oi} l_{ef} + B_S b_{ii} l_{ef} + \frac{B_S b_{ii} l_{ef} R_{ib}}{R_{nbhi}//R_{bi}}\right) i_s \sin\beta \end{aligned} \tag{40}$$

$$k_{s1} = \frac{\psi_{pm}}{\left(2L_{dd} + l_{aal}\right) i_s} = \frac{N\left(\frac{F_{pm1}+F_{pm2}+F_{pm3}}{R_{gd}+R_{\mathrm{barrier}}//R_{\mathrm{bridge}}+R_{drib}} + 2B_S b_{oi} l_{ef} + B_S b_{ii} l_{ef} + \frac{B_S b_{ii} l_{ef} R_{ib}}{R_{nbhi}//R_{bi}}\right)}{\left(\frac{3N^2}{\frac{8\delta}{\pi\mu_0 l_{ef} r} + R_{rd}} + l_{aal}\right) i_s} \tag{41}$$

$$k_{s2} = \frac{\psi_{pm}}{\left(L_{dd} + l_{aal}\right) i_s} = \frac{N\left(\frac{F_{pm1}+F_{pm2}+F_{pm3}}{R_{gd}+R_{\mathrm{barrier}}//R_{\mathrm{bridge}}+R_{drib}} + 2B_S b_{oi} l_{ef} + B_S b_{ii} l_{ef} + \frac{B_S b_{ii} l_{ef} R_{ib}}{R_{nbhi}//R_{bi}}\right.}{\left(\frac{1.5N^2}{\frac{8\delta}{\pi\mu_0 l_{ef} r} + R_{rd}} + l_{aal}\right) i_s}. \tag{42}$$

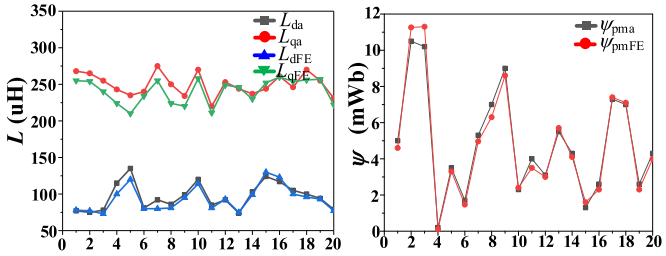

Fig. 7. Comparison of analytical and FE calculation results.

and rotor path magnetomotive force can be calculated

$$F_l = \sum_{i=1}^{3} (F_{pmi}) \left(1 - \frac{R_{\text{bridge}}}{R_{gd} + R_{\text{barrier}} // R_{\text{bridge}} + R_{drp}}\right) \tag{50}$$

$$F_{rp} = \frac{\sum_{i=1}^{3} (F_{pmi})\, R_{drp}}{R_{gd} + R_{\text{barrier}} // R_{\text{bridge}} + R_{drp}} \tag{51}$$

where F_l is the barrier magnetomotive force and F_{rp} is rotor path magnetomotive force. Furtherly, magnetic bridge saturation magnetic density B_{s} and rotor path magnetic density B_{n} can be calculated

$$B_S = \frac{F_{li}}{A_{\text{bridge}}\, R_{\text{bridge}}} \tag{52}$$

$$B_n = \frac{F_{rp}}{A_{rp}\, R_{rp}} \tag{53}$$

where A_{bridge} is the area of the magnetic bridge and A_{rp} is the area of the rotor path. μ_{s} and μ_{n} can be obtained by rotor material BH curve at B_{s} and B_{n}. If $|\mu_{\text{s}}\text{-}\mu_{\text{s}}'| > \varepsilon$ or $|\mu_{\text{n}}\text{-}\mu_{\text{n}}'| > \varepsilon$, assume μ_{s}', μ_{n}' again until $|\mu_{\text{s}}\text{-}\mu_{\text{s}}'| < \varepsilon$, and $|\mu_{\text{n}}\text{-}\mu_{\text{n}}'| < \varepsilon$. By now, μ_{s}' and μ_{n}' can be regarded as μ_{s} and μ_{n}. According to μ_{s} and μ_{n}, the *dq*-axis inductance and permanent magnet flux can be calculated.

In total, 20 groups of rotor structure parameters are selected randomly, and *dq*-axis inductance and flux are calculated by the method of analytical model and FE model, respectively, as shown in Fig. 7, where L_{da}, L_{qa}, ψ_{pma} is analytical calculation results of *dq*-axis inductance and flux and L_{dFE}, L_{qFE}, ψ_{pmFE} are FE calculation results of that. The results of analytical calculation are close to that of FE calculation, which means analytical model proposed in this article is credible.

Therefore, the analysis results of the L_{d}-L_{q}, ρ, i_s (rated current), k_{sc} (ratio of single-three-phase short circuit current to rated current), λ (ratio of permanent magnet torque to rated electromagnetic torque), and $|\cos\varphi|$ (power factor) can be regarded as credible.

2) Magnetic Barrier Size: Three-layer magnetic barrier rotor structure is adopted. Each layer thickness change affects the total electromagnetic performance. For better description of the relationship and influence, total magnetic barrier thickness is analyzed first, good electromagnetic performance is obtained and further, the influence of each layer magnetic barrier thickness on electromagnetic performance is discussed.

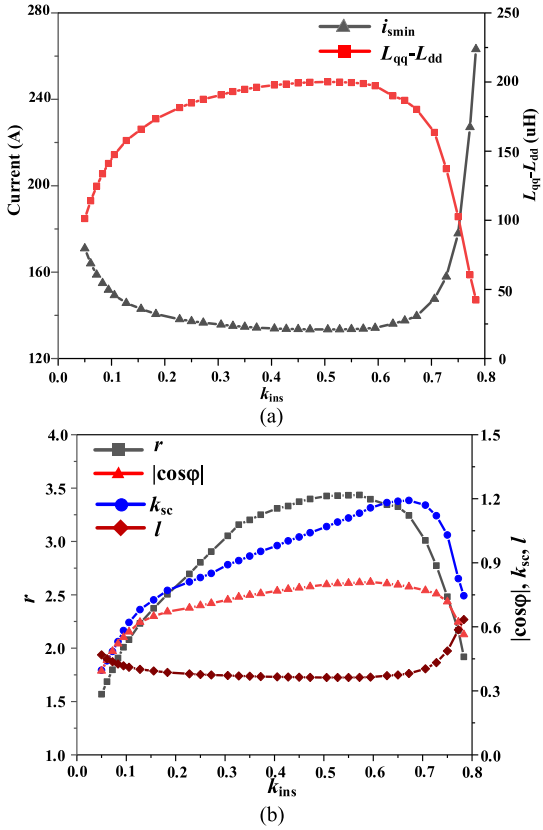

Fig. 8. Influence between electromagnetic performance and the minimum current of each k_{ins}.

First, the insulation ratio k_{ins} is introduced, i.e., the ratio of the total equivalent thickness of three-layer magnetic barriers to the rotor radial thickness. According to the principle of constant equivalence of magnetic barrier reluctance, the equivalent thickness is carried out

$$h_{eqi} = \frac{b_{pi} h_{pmi} + b_{bi} h_{bi}}{b_{bi} + b_{pmi}} \tag{54}$$

and

$$k_{ins} = \sum_{i=1}^{3} \frac{h_{eqi}}{r_r}. \tag{55}$$

During the analysis, some initial conditions are set as: the sum of the thickness of each layer rotor path and each layer magnetic barrier is a constant value *m*, the thickness of the magnetic bridge and the width of the permanent magnet is constant value, the thickness of the permanent magnet is equal to the thickness of the horizontal magnetic barrier. Only the thickness of the horizontal magnetic barrier and the inclined magnetic barrier are changed. With different magnetic barrier parameters, the minimum current required by rated power generation electromagnetic torque can be obtained by MTPA.

Fig. 8(a) and (b) shows the relationship between electromagnetic performance and the minimum current of each k_{ins}.

From Fig. 8(a), when k_{ins} is in the range of 0.4–0.6, the difference of *dq*-axis inductance (L_{qq}-L_{dd}) is higher than the condition of $k_{\text{ins}} > 0.6$ or $k_{\text{ins}} < 0.4$, which results in lower current needed

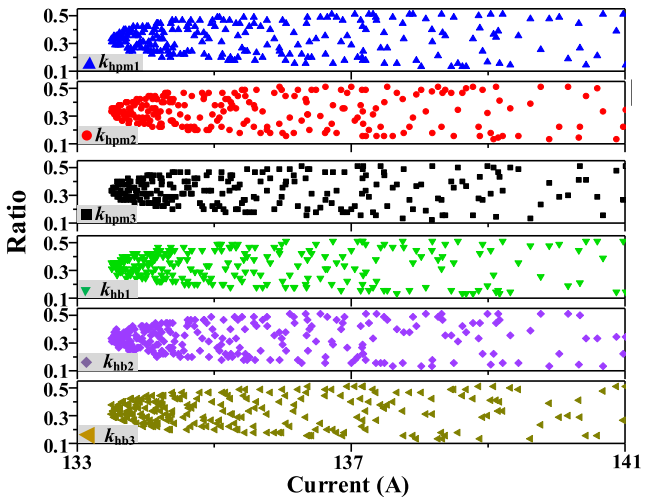

Fig. 9. $k_{ins} = 0.5$, the relationship between the rated current and k_{hpm1}, k_{hpm2}, k_{hpm3}, k_{hb1}, k_{hb2}, k_{hb3}.

for rated torque. High torque-current ratio and good performance can be obtained in this range. However, when k_{ins} is <0.4 or k_{ins} >0.6, the difference of *dq*-axis inductance decreases, rated current increases fast, torque-current ratio decreases fast, and the performance operates worse.

From Fig. 8(b), with the increase of k_{ins}, $|\cos\varphi|$, ρ, k_{sc}, and λ increase first and decrease. When k_{ins} is in the range of 0.45–0.65, high salient pole ratio and power factor can be obtained and the performance is not sensitive to the change of k_{ins}.

Therefore, when k_{ins} is in the range of 0.45–0.6, the PMaSynR SG can obtain electromagnetic performance of high difference of *dq*-axis inductance and high salient pole ratio and high power factor and high torque-current ratio.

Fig. 9 shows at the condition of $k_{ins} = 0.5$, the relationship between the rated current and the ratio of each layer thickness of magnetic barrier to the three-layer total thickness, where, $k_{hpm1}, k_{hpm2}, k_{hpm3}, k_{hb1}, k_{hb2}, k_{hb3}$ is the ratio of the magnetic barrier thickness of each layer to the total three-layer equivalent thickness (for example, $k_{hpm1} = h_{pm1}/(h_{eq1} + h_{eq2} + h_{eq3})$). Every column in Fig. 9 is one set of parameters of k_{hpm1}, k_{hpm2}, k_{hpm3}, k_{hb1}, k_{hb2}, and k_{hb3} corresponding to certain current. When the ratio of each layer magnetic barrier thickness to the total three-layer magnetic barrier thickness is all in the range of 0.3–0.35, high torque-current ratio and good electromagnetic performance can be obtained. And in this range, they are insensitive to the change of the ratios. When the ratios are away from the range of 0.3–0.35, the rated current increases, the ratio of torque to current, and output performance decreases, and they are significantly influenced by the change of the ratios.

3) Magnetic Bridge Size: The influence of the outer and inner magnetic bridge on both electromagnetic and mechanical performances of PMaSynR SG are studied. According to last part analysis of k_{ins}, $k_{ins} = 0.5$ is selected and the ratio of each layer thickness to total three thickness k_{hpm1}, k_{hpm2}, and k_{hpm3} is selected as 0.34, 0.33, and 0.33.

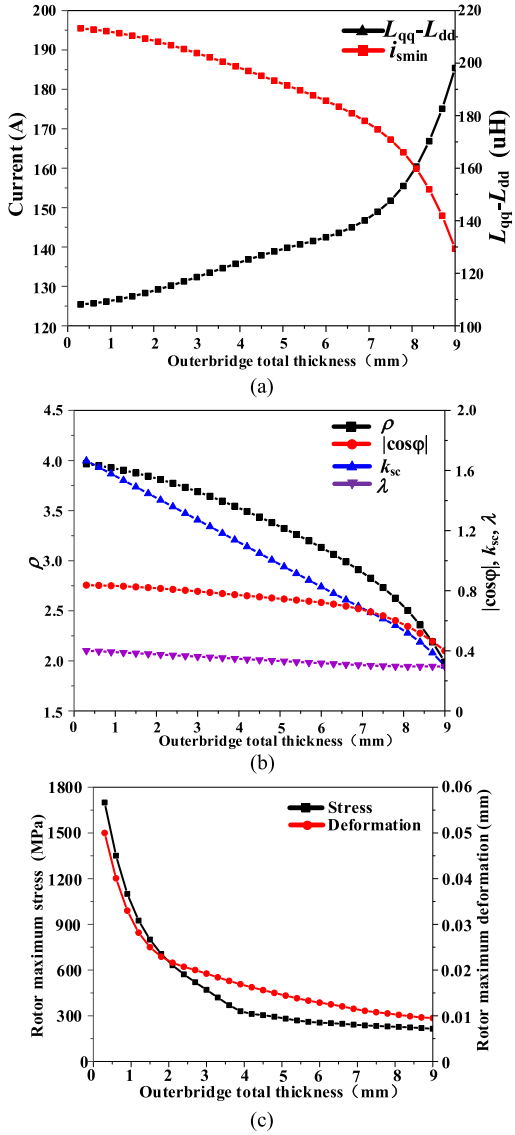

Fig. 10. Influence between outer bridge thickness and PMaSynR SG performance.

First, the inner magnetic bridge thickness is kept constant, only each layer outer magnetic bridge thickness changes. Different outer magnetic bridge thickness combinations can obtain different rated current and different torque-current ratio. The electromagnetic and mechanical performance at minimum rated current value (maximum torque-current ratio) of each three-layer outer magnetic bridge total thickness are selected to draw Fig. 10.

Fig. 10(a) and (b) is the relationship between outer magnetic bridge total thickness and electromagnetic performance. With the increase of outer magnetic bridge thickness, the difference of *dq*-axis inductance ρ, $|\cos\varphi|$ k_{sc} decreases, rated current increases, and torque-current ratio decreases. When the outer magnetic bridge total thickness is more than 7 mm, the electromagnetic performance decreases significantly.

Fig. 10(c) shows the relationship between outer magnetic bridge total thickness and mechanical performance of maximum

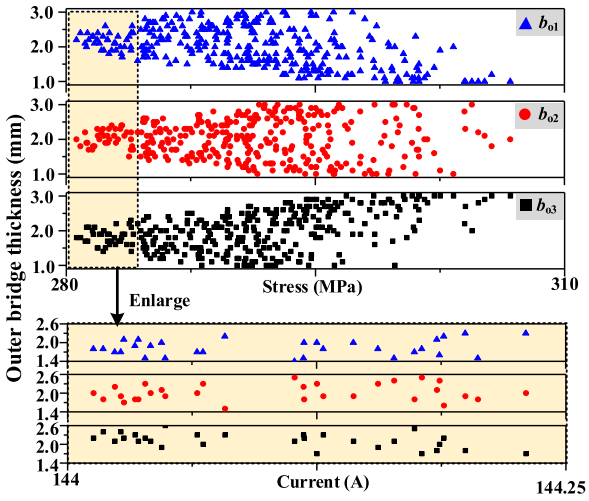

Fig. 11. Influence between each layer outer magnetic bridge thickness and PMaSynR SG performance.

stress and deformation. When the outer magnetic bridge total thickness is more than 4 mm, the maximum stress of the rotor is less than 300 MPa (set 2 times safety margin) and decreases slowly. The design range of outer magnetic bridge total thickness is 4–7 mm.

Fig. 11 shows at the outer magnetic bridge total thickness of 6 mm, the relationship between different combinations of each layer outer magnetic bridge thickness and electromagnetic and mechanical performance. Every column in Fig. 11 is one set of parameters of b_{o1}, b_{o2}, b_{o3} corresponding to certain stress or current. The enlarged figure in Fig. 11 is the rated current of different combinations with the stress range of 280–285 MPa. When each layer outer magnetic bridge thickness is similar and $b_{o1} > b_{o2} > b_{o3}$, good electromagnetic and mechanical performance can be obtained.

The analysis of inner magnetic bridge thickness is similar to that of the outer magnetic bridge thickness. A combination of three-layer outer magnetic bridge thickness with the total thickness of 6 mm is selected and only inner magnetic bridge thickness changes. Different inner magnetic bridge thickness combinations can obtain different rated current. The electromagnetic and mechanical performance at minimum rated current value (maximum torque-current ratio) of each three-layer inner magnetic bridge total thickness are selected to draw Fig. 12.

Fig. 12(a) and (b) is the relationship between inner magnetic bridge total thickness and electromagnetic performance. With the increase of inner magnetic bridge thickness, the difference of dq-axis inductance ρ, $|\cos\varphi|$ k_{sc} decreases, rated current increases, and torque-current ratio decreases. When the inner magnetic bridge total thickness is more than 6 mm, the electromagnetic performance decreases significantly.

Fig. 12(c) shows the relationship between inner magnetic bridge total thickness and mechanical performance of maximum stress and deformation. With the inner magnetic bridge total thickness is more than 4.5 mm, the maximum stress of the rotor is less than 300 MPa and decreases slowly.

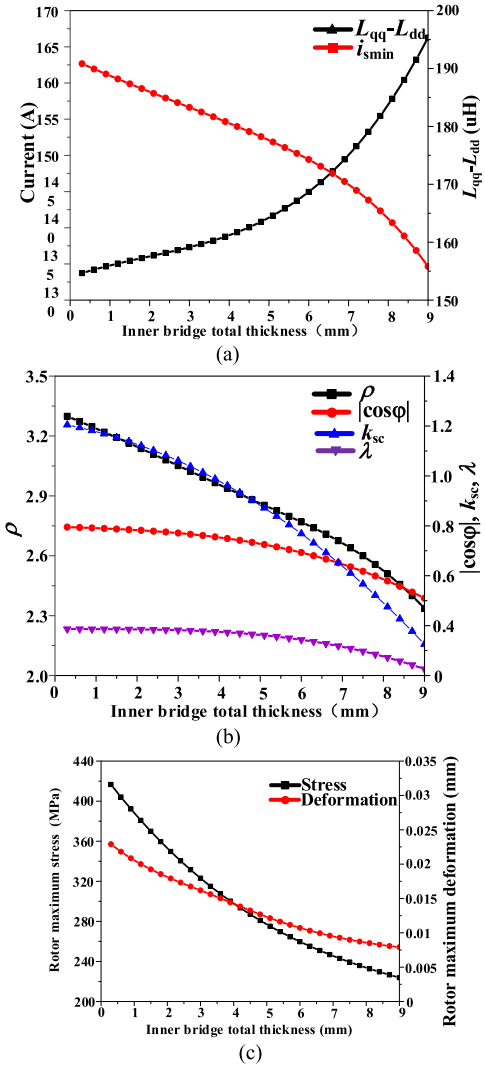

Fig. 12. Influence between inner bridge thickness and PMaSynR SG performance.

The design range of inner magnetic bridge total thickness is 4.5–6 mm.

Fig. 13 shows at the inner magnetic bridge total thickness of 5 mm, the relationship between different combinations of each layer inner magnetic bridge thickness and electromagnetic and mechanical performance. Every column in Fig. 13 is one set of parameters of b_{i1}, b_{i2}, b_{i3} corresponding to certain stress or certain current. The enlarged figure in Fig. 13 is the rated current of different combinations with the stress range of 260–270 MPa. When each layer inner magnetic bridge thickness is similar and $b_{i1} > b_{i2} > b_{i3}$, good electromagnetic and mechanical performance can be obtained.

4) Permanent Magnet Size: For fulfilling the reliability requirements of the aviation starter generator system, it is essential to ensure that the short circuit current will not cause the PMaSynR SG overheat. The short circuit current is determined by d-axis inductance and permanent magnet flux. The size range of magnetic barrier and magnetic bridge with good electromagnetic performance is given above, which means the design

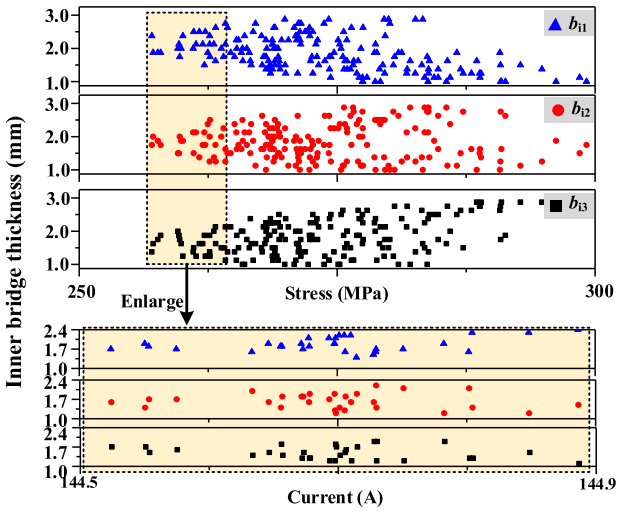

Fig. 13. Influence between each layer inner magnetic bridge thickness and PMaSynR SG performance.

range of *dq*-axis inductance is determined. The analysis of the influence of permanent magnet flux on short-circuit current and electromagnetic performance is discussed in this part. The permanent magnet adopts cuboid structure and is embedded in the horizontal magnetic barriers. The thickness is equal to that of the horizontal magnetic barrier.

For convenience of the description of the relationship between the volume of permanent magnet and the antishort-circuit ability and electromagnetic performance, k_{pm} is defined as the ratio of the total permanent magnet volume to the total horizontal magnetic barrier volume

$$k_{pm} = \frac{b_{pm1}h_{pm1} + b_{pm2}h_{pm2} + b_{pm3}h_{pm3}}{b_{bp1}h_{pm1} + b_{bp2}h_{pm2} + b_{bp3}h_{pm3}}. \tag{56}$$

A combination of magnetic barrier and magnetic bridge parameters with good electromagnetic and mechanical performance is selected and is kept constant, only the width of each layer permanent magnet changes. The combination of permanent magnet width with minimum rated current (maximum torque-current ratio) at each k_{pm} is selected to draw Fig. 14.

Fig. 14(a) and (b) shows the relationship between $k_{\rm pm}$ and electromagnetic performance. With the increase of the volume of permanent magnet, electromagnetic performance is significantly improved, followed by the increase of short-circuit current. When k_{pm} is 0.82, the short circuit current is equals to rated current.

Fig. 15 shows at the condition of $k_{pm} = 0.75$, the relationship between the different width of each layer permanent magnet and the rated current, where, $k_{\rm bpm1}$, $k_{\rm bpm2}$, $k_{\rm bpm3}$ is the ratio of each layer permanent magnet volume to the located-layer horizontal magnetic barrier volume. Every column in Fig. 15 is one set of parameters of $k_{\rm bpm1}$, $k_{\rm bpm2}$, $k_{\rm bpm3}$ corresponding to certain current. When $k_{\rm bpm1}$, $k_{\rm bpm2}$, and $k_{\rm bpm3}$ are in the range of 0.65–0.85, the higher torque-current ratio and better electromagnetic performance can be obtained and they are insensitive to the change of the ratios.

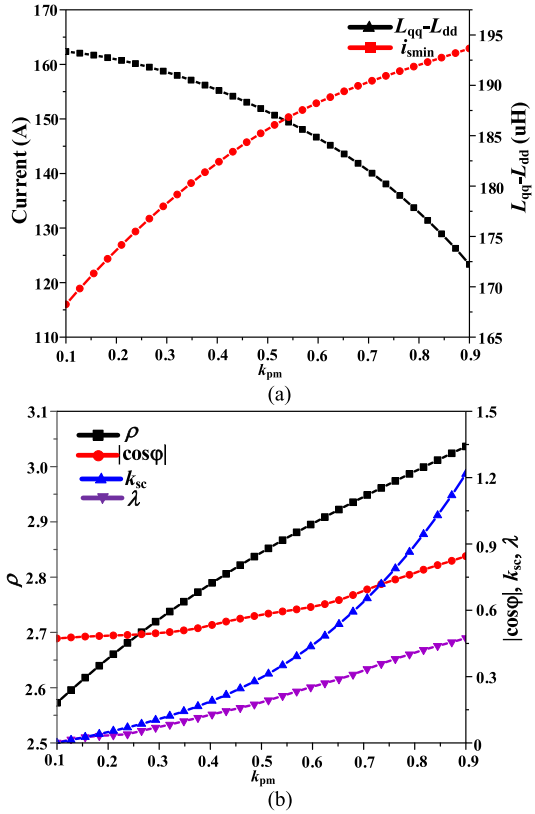

Fig. 14. Influence between k_{pm} and PMaSynR SG performance.

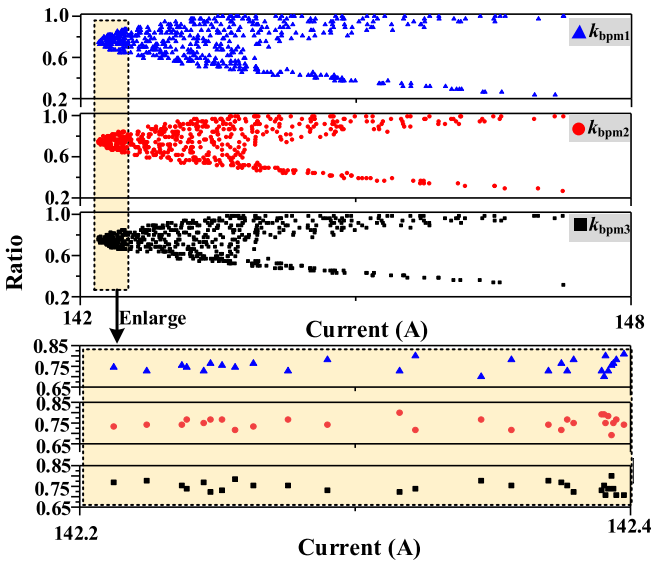

Fig. 15. Influence between $k_{\rm bpm1}$, $k_{\rm bpm2}$, $k_{\rm bpm3}$ and PMaSynR SG performance.

In this section, *dq*-axis inductance and permanent magnet flux linkage are derived, and the influence on the electromagnetic performance and antishort-circuit ability is discussed.

IV. Simulation Calculation

According to basic parameter selection and the influence of rotor structure parameters on output performance and

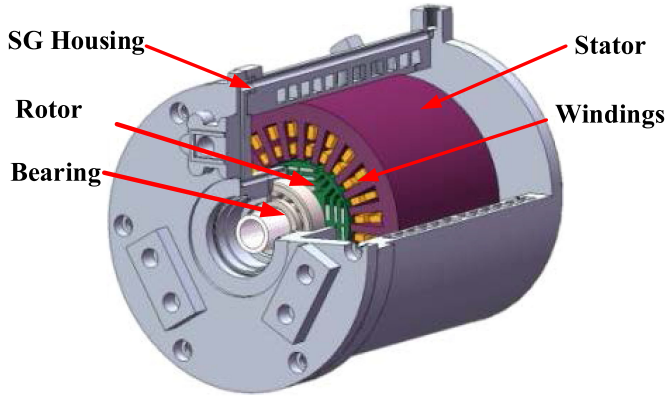

Fig. 16. PMaSynR SG model.

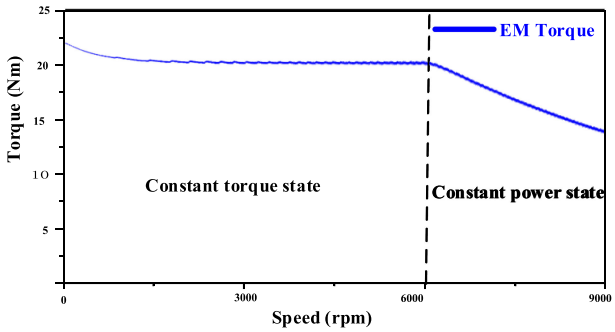

Fig. 17. Torque-speed at starting process.

antishort-circuit ability mentioned previously, a 24 000 r/min, 40 kW PMaSynR SG is designed shown in Fig. 16.

The PMaSynR SG is controlled by the power converter the starting and power generation processes with the method of MTPA.

A. Starting State

During starting process, PMaSynR SG starts with load of 20 N•m to 6000 r/min, and then runs to 9000 r/min with the load of 12.56 kW constant power. The simulation results of starting process are shown in Fig. 17.

B. Power Generation State

Fig. 18 shows the no load back EMF waveform at 24 000 r/min, and the amplitude is 91 V.

Fig. 19(a) and (b) shows 270 V dc voltage at 24 000 r/min at no-load and rated power generation, respectively. The ripple is 0.3 V at no-load power generation and 0.4 V at rated power generation.

Fig. 20(a) and (b) shows the magnetic density distribution at no-load and rated power generation. At no load power generation, the main magnetic circuit is unsaturated, while the magnetic bridge is highly saturated. At rated power generation, the main magnetic circuit of stator yoke and rotor is wide and unsaturated, while the teeth are narrow and partially saturated, but it has little influence on the overall electromagnetic performance.

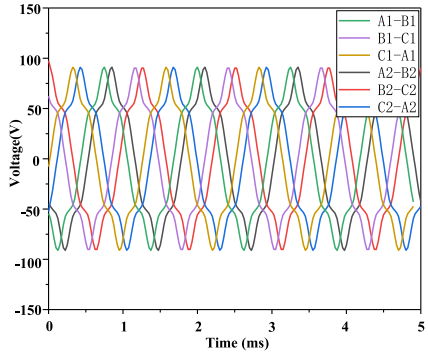

Fig. 18. No load back EMF waveform at 24 000 r/min.

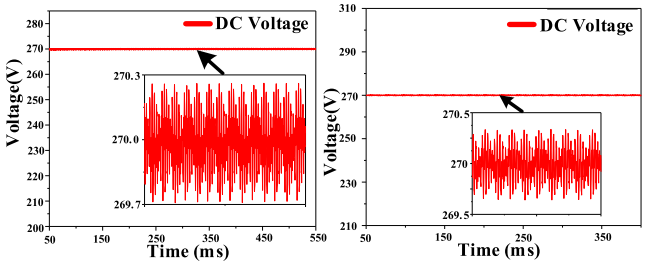

Fig. 19. 270 V dc voltage and ripple. (a) 270 V DC (ripple = 0.3 V) @ Noload. (b) 270 V DC (ripple = 0.4 V) @ Rated power generation.

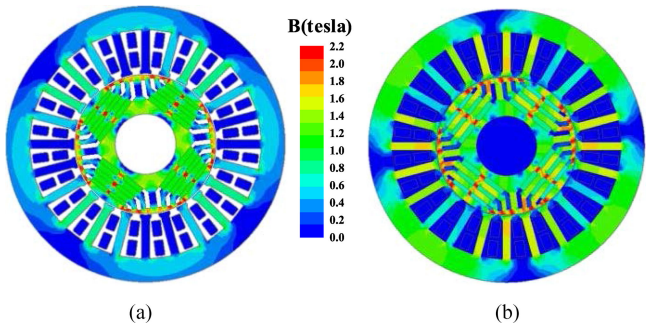

Fig. 20. Magnetic density distribution. (a) Flux Density @ No-load. (b) Flux Density @ Rated power generation.

Fig. 21(a) and (b) shows the short-circuit current of single-three-phase and dual-three-phase, i_{sc1} rms and i_{sc2} rms is 75 A and 57 A, respectively. The rated current rms is 113.5 A. The maximum short-circuit current is 66% of the rated value, which will not cause the PMaSynR SG to overheat.

Through the analysis of starting process, no-load power generation, rated power generation, and short circuit fault, the proposed PMaSynR SG has strong antishort-circuit ability and excellent electromagnetic performance.

V. Experiment

The dual-three-phase 40 kW/24 000 r/min PMaSynR SG prototype is manufactured (as shown in Fig. 22) with the weight of 13 kg and with the heat-dissipating method of oil spraying.

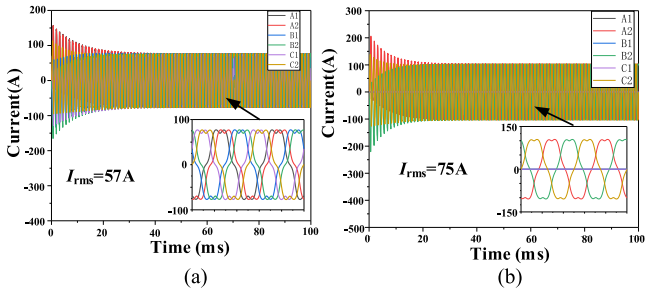

Fig. 21. Short-circuit current waveform. (a) Dual-Three-Phase Short-Circuit. (b) Single-Three-Phase Short-Circuit.

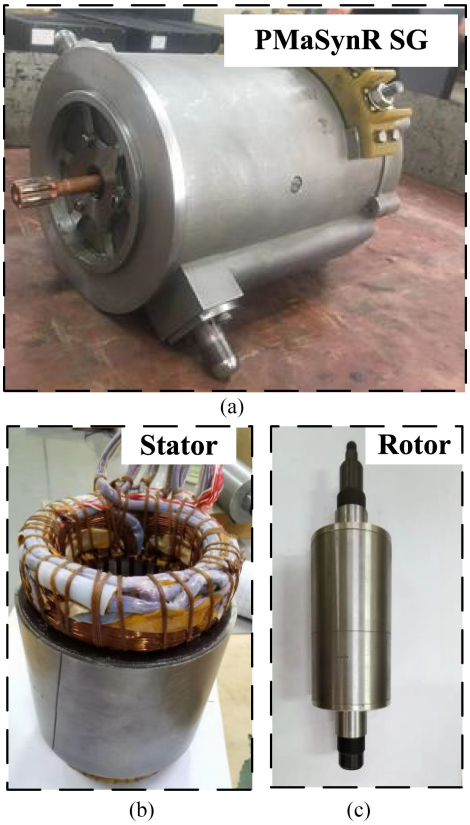

Fig. 22. PMaSynR SG prototype. (a) PMaSynR SG prototype. (b) Stator and winding. (c) Rotor.

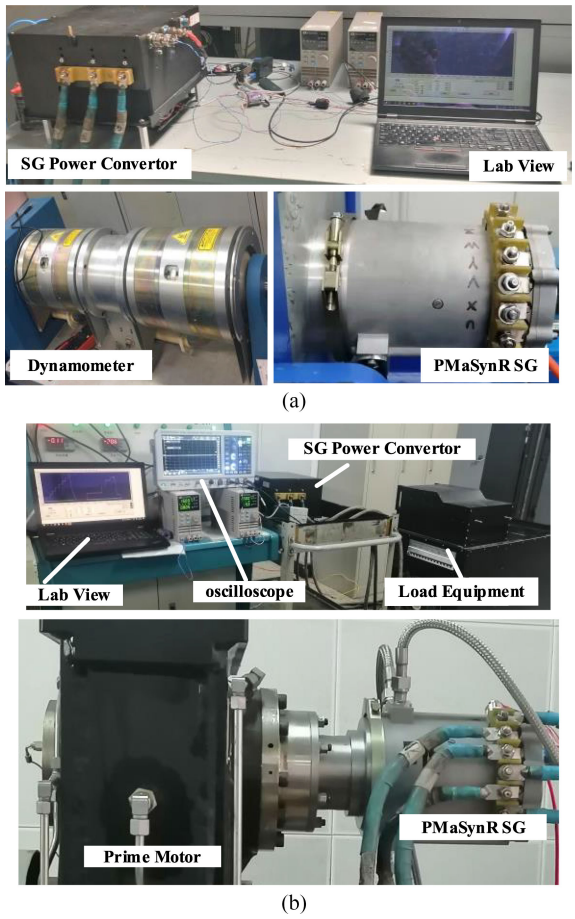

Fig. 23. Starting and power generation experiment platforms. (a) Starting process platform. (b) Power generation platform.

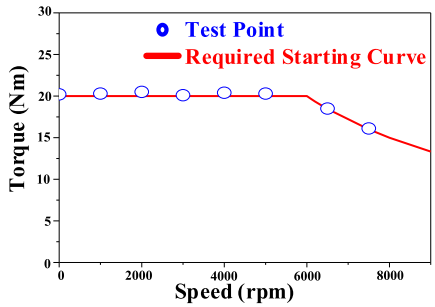

Fig. 24. PMaSynR SG load capacity test during starting process.

Experiments of starting, power generation and short circuit fault are carried out.

The starting and power generation experiment platforms are constructed, as shown in Fig. 23. Fig. 23(a) shows that the starting experiment platform is composed of PMaSynR SG, SG power converter, and dynamometer. Fig. 23(b) shows that the power generation experimental platform is composed of prime motor, PMaSynR SG, SG power converter, and load equipment.

A. Starting State Experiment: Fig. 24 shows the PMaSynR SG load capacity test results during starting process. From the results, PMaSynR SG can meet the requirements of 0–6000 r/min at constant torque (20 N•m) operation and 6000–9000 r/min constant power operation.

B. Power Generation State Experiment

Fig. 25 shows the experimental results of PMaSynR SG performance at different load and speed. Fig. 25(a) shows the no-load line voltage back EMF at 24 000 r/min, and the amplitude of experimental result is 2.1% lower than that of the simulation result. Fig. 25(b) shows that the output dc voltage is 270 V $\pm$ 1.5 V at no-load power generation. Fig. 25(c1) and (c2) shows the phase current of PMaSynR SG and the output dc voltage (270 V $\pm$ 2.8 V) at 12 000 r/min/20 kW resistance load, and the phase current rms of experimental result is 5.5% higher than that of the simulation result. Fig. 25(d1) and (d2) shows the phase current of PMaSynR SG and the output dc voltage (270 V

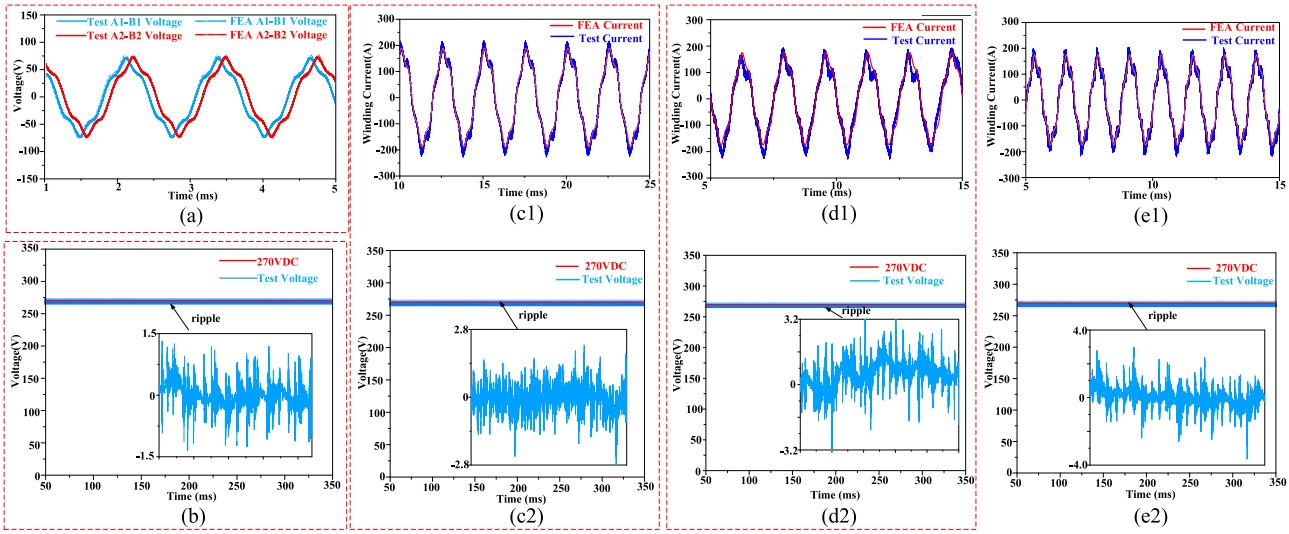

Fig. 25. Experimental results of PMaSynR SG performance at no-load, different rated power generation. (a) No-load Back EMF. (b) 270 VDC@No-load(ripple = 1.5 V).

TABLE III
EFFICIENCY AT DIFFERENT SPEED

Speed(rpm)	Load Power(kW)	Experiment Efficiency (%)	Simulation Efficiency (%)
6000	10	85.7	88.1
9000	15	92.9	94.0

$\pm$ 3.2 V) at 18 000 r/min/30 ;kW resistance load, and the phase current rms of experimental result is 5.3% higher than that of the simulation result. Fig. 25(e1) and (e2) shows the phase current of PMaSynR SG and the output dc voltage (270 V $\pm$ 3.8 V) at 24 000 r/min/40 kW resistance load, and the phase current rms of experimental result is 4.8% higher than that of the simulation result.

The experimental results abovementioned show that within the allowable error range, the design of the 40 kW/24 000 r/min PMaSynR SG is accurate, and the output performance can meet the requirements. In spite that the voltage ripple of the experiment is higher than that of the simulation, it is mainly affected by the parasitic parameters of the power converter, and it is out of the research content in this article. The voltage ripple shown in this article aims to illustrate that the proposed PMaSynR SG has the capability of voltage regulation at power generation.

The efficiency of PMaSynR SG at different power generation conditions is tested and shown in Table III.

From Table III, the experimental efficiency is slightly lower than the simulation results, mainly because the core loss caused by the high-order harmonics of the power tube switching is ignored in the simulation, and the experimental core and copper loss is higher than simulation value. However, there is little difference between simulation value and experiment value, which proves that the efficiency calculation is reliable. Therefore, the simulation efficiency is 96.5% at 40 kW/24 000 r/min power generation, and through comprehensive analysis, the actual efficiency can reach 94%.

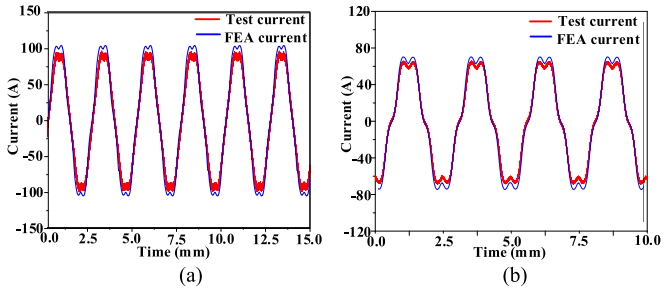

Fig. 26. Experimental results of short-circuit current. (a) Single-three-phase short circuit fault. (b) Dual-three-phase short circuit fault.

C. Short-Circuit Fault Experiment

Fig. 26 shows the experimental results of the short-circuit current of PMaSynR SG. Fig. 26(a) and (b) shows the single-three-phase and dual-three-phase short-circuit current, and the rms value is 70 A and 53 A, respectively. The ratio of single-three-phase short-circuit current to rated current is 59%. Because the end leakage inductance is ignored in the simulation, the actual dq-axis inductance is higher, resulting in lower short-circuit current. Meanwhile, the experiment rated current is higher than the simulation value, resulting in lower k_s. Due to the little difference of value between experiment and simulation, it can be considered that the design is accurate, and PMaSynR SG has strong antishort-circuit ability.

From the abovementioned experiments, the proposed PMaSynR SG has excellent electromagnetic performance of high efficiency, high power density, and strong antishort-circuit ability.

VI. CONCLUSION

In this article, a novel aviation dual-three-phase PMaSynR SG is proposed. The design method of PMaSynR SG with high electromagnetic performance and excellent antishort-circuit

ability is proposed, and the main PMaSynR SG parameters selection is given. The influence of rotor structure parameters on electromagnetic performance and antishort-circuit ability is clarified by establishing the simplified *dq*-axis equivalent magnetic circuit model and the parameter sensitivity analysis. The following conclusions can be drawn.

1) The *dq*-axis inductance difference, the salient pole ratio ρ, the power factor $|\cos\varphi|$ and the short-circuit/rated current ratio $k_{\rm sc}$ increases first and then decreases as the insulation ratio of magnetic barrier $k_{\rm ins}$ increases. For $k_{\rm ins}$ in the range of 0.45–0.6 and the ratio of each magnetic barrier thickness to total magnetic barrier thickness in the range of 0.3–0.35, the high *dq*-axis inductance difference, the high salient pole ratio ρ, the high power factor $|\cos\varphi|$, and the high torque-current ratio can be obtained for the PMaSynR SG.
2) As the total thickness of outer and inner magnetic bridge increase, the electromagnetic performance of the PMaSynR SG becomes worse but the mechanical performance gets better. Furthermore, both the electromagnetic and the mechanical performance can be guaranteed for the outer magnetic bridge total thickness in the range of 4–7 mm, the thickness of each layer of outer magnetic bridge relatively close with $b_{\rm o1} > b_{\rm o2} > b_{\rm o3}$, the inner magnetic bridge total thickness in the range of 4–6 mm, and the thickness of each layer of inner magnetic bridge relatively close with $b_{\rm i1} > b_{\rm i2} > b_{\rm i3}$.
3) With the increase of the permanent magnet, the electromagnetic performance of the PMaSynR SG becomes better, while the short-circuit current increases as well. When the ratio of total volume of the permanent magnet to the total horizontal magnetic barrier volume is less than 0.82, the short-circuit current of the PMaSynR SG can be less than its rated current. In addition, the electromagnetic performance of the PMaSynR SG can get better when the ratio of each layer volume of permanent magnet to the volume of horizontal magnetic barrier k_{pm1}, k_{pm2}, k_{pm3} is close to k_{pm}.

Finally, a 40 kW/24 000 r/min PMaSynR SG prototype is manufactured with the characteristics of high efficiency (94%), high power density (3.1 kW/kg), and strong antishort-circuit ability (the short-circuit current is only 59% of the rated value).

The novelty of this article is to be the first time to propose a high-speed high-power dual-three-phase PMaSynR SG in aerospace application with the antishort-circuit capacity, and the feasibility of the PMaSynR SG applied in aerospace starter generator power system is verified by theory and experiment. It provides a guideline and a novel research direction for engineers to follow in aviation high-power high-speed starter-generator system field.

REFERENCES

[1] Z. Liu, K. Wang, H. Sun, J. Li, and B. Zhou, "DC-field excitation variable flux reluctance," *IEEE Trans. Ind. Electron.*, vol. 68, no. 8, pp. 6444–6455, Aug. 2021.

[2] S. Bozhko *et al.*, "Development of aircraft electric starter-generator system based on active rectification technology," *IEEE Trans. Transp. Electrific.*, vol. 4, no. 4, pp. 985–996, Dec. 2018.

[3] B. Sarlioglu and C.T. Morris, "More electric aircraft: Review, challenges, and opportunities for commercial transport aircraft," *IEEE Trans. Transp. Electrific.*, vol. 1, no. 1, pp. 54–64, Jun. 2015.

[4] X. Zhou, B. Zhou, K. Wang, L. Zhang, and Y. Zhao, "Two-step rotor position estimation method for doubly salient electromagnetic starter-generator over zero and low speeds range," *IEEE J. Emerg. Sel. Topics Power Electron.*, vol. 9, no. 3, pp. 2664–2673, Jun. 2021.

[5] T. Meng, W. Liu, N. Jiao, X. Han, R. Wang, and Y. Jiang, "Rotor position estimation for aviation three-stage starter/generators in the low-speed region without high-frequency signal injection," *IEEE Trans. Power Electron.*, vol. 35, no. 8, pp. 8405–8416, Aug. 2020.

[6] H. Liu *et al.*, "Control strategy for five-phase dual-stator winding induction starter/generator system," *IEEE Trans. Ind. Electron.*, vol. 67, no. 4, pp. 2607–2617, Apr. 2020.

[7] Y. Xu, Z. Zhang, Z. Bian, and L. Yu, "Copper loss optimization based on bidirectional converter for doubly salient brushless starter/generator system," *IEEE Trans. Ind. Electron.*, vol. 68, no. 6, pp. 4769–4779, Jun. 2021.

[8] J. K. Noland, M. Leandro, J.A. Suul, and M. Molinas, "High-power machines and starter-generator topologies for more electric aircraft: A technology outlook," *IEEE Access*, vol. 8, no. 1, pp. 130104–130123, Jul. 2020.

[9] X. Lang, T. Yang, C. Li, H.B. Enalou, S. Bozhko, and P. Wheeler, "A dual-channel enhanced power generation architecture with back-to-back converter for MEA application," *IEEE Trans. Ind. Appl.*, vol. 56, no. 3, pp. 3006–3019, May/Jun. 2020.

[10] J. Pang, W. Liu, Z. Wei, C. Sun, N. Jiao, and X. Han, "Online diode fault detection in rotating rectifier of the brushless synchronous starter generator," *IEEE Trans. Ind. Inform.*, vol. 16, no. 11, pp. 6943–6951, Nov. 2020.

[11] J. Wei, H. Xu, B. Zhou, Z. Zhang, and C. Gerada, "An integrated method for three-phase AC excitation and high-frequency voltage signal injection for sensorless starting of aircraft starter/generator," *IEEE Trans. Ind. Electron.*, vol. 66, no. 7, pp. 5611–5622, Jul. 2019.

[12] S. Song, R. Hei, R. Ma, and W. Liu, "Model predictive control of switched reluctance starter/generator with torque sharing and compensation," *IEEE Trans. Transp. Electrific.*, vol. 6, no. 4, pp. 1519–1527, Dec. 2020.

[13] J.B. Bartolo, M. Degano, J. Espina, and C. Gerada, "Design and initial testing of a high-speed 45-kW switched reluctance drive for aerospace application," *IEEE Trans. Ind. Electron.*, vol. 64, no. 2, pp. 988–997, Feb. 2017.

[14] S. S. Yeoh, T. Yang, L. Tarisciotti, C. I. Hill, S. Bozhko, and P. Zanchetta, "Permanent-magnet machine-based starter-generator system with modulated model predictive control," *IEEE Trans. Transp. Electrific.*, vol. 3, no. 4, pp. 878–890, Dec. 2017.

[15] L. Rovere, A. Formentini, G. L. Calzo, P. Zanchetta, and T. Cox, "Zero-sequence voltage elimination for dual-fed common DC-link open-end winding PMSM high-speed starter-generator—Part I: Modulation," *IEEE Trans. Ind. Appl.*, vol. 55, no. 6, pp. 7804–7812, Nov./Dec. 2019.

[16] N. Fernando, G. Vakil, P. Arumugam, E. Amankwah, C. Gerada, and S. Bozhko, "Impact of soft magnetic material on design of high-speed permanent-magnet machines," *IEEE Trans. Ind. Electron.*, vol. 64, no. 3, pp. 2415–2423, Mar. 2017.

[17] I. Boldea, L. N. Tutelea, L. Parsa, and D. Dorrell, "Automotive electric propulsion systems with reduced or no permanent magnets: An overview," *IEEE Trans. Ind. Electron.*, vol. 61, no. 10, pp. 5696–5711, Oct. 2014.

[18] M. Barcaro, N. Bianchi, and F. Magnussen, "Permanent-magnet optimization in permanent-magnet-assisted synchronous reluctance motor for a wide constant-power speed range," *IEEE Trans. Ind. Electron.*, vol. 59, no. 6, pp. 2495–2502, Jun. 2012.

[19] M. Zhao, G. Liu, Q. Chen, W. Zhao, and C. H. T. Lee, "Fault-tolerant control of a triple redundant PMA-SynRM driven under single-phase open-circuit by mono-inverter," *IEEE Trans. Power Electron.*, vol. 36, no. 10, pp. 11593–11605, Oct. 2021.

[20] Y. Lu *et al.*, "Comparative study on vibration behaviors of permanent magnet assisted synchronous reluctance machines with different rotor topologies," *IEEE Trans. Ind. Appl.*, vol. 57, no. 2, pp. 1420–1428, Mar./Apr. 2021.

[21] Y. Wang, G. Bacco, and N. Bianchi, "Geometry analysis and optimization of PM-assisted reluctance motors," *IEEE Trans. Ind. Appl.*, vol. 53, no. 5, pp. 4338–4347, Sep./Oct. 2021.

[22] D. K. Ngo, M.F. Hsieh, and T. A. Huynh, "Torque enhancement for a novel flux intensifying PMa-SynRM using surface-inset permanent magnet," *IEEE Trans. Magn.*, vol. 55, no. 7, Jul. 2019, Art. no. 8106108.

[23] M. Degano, E. Carraro, and N. Bianchi, "Selection criteria and robust optimization of a traction PM-assisted synchronous reluctance motor," *IEEE Trans. Ind. Appl.*, vol. 51, no. 6, pp. 4383–4391, Nov./Dec. 2015.

[24] W. Wu, X. Zhu, L. Quan, Y. Du, Z. Xiang, and Z. Zhu, "Design and analysis of a hybrid permanent magnet assisted synchronous reluctance motor considering magnetic saliency and PM usage," *IEEE Trans. Appl. Supercond.*, vol. 28, no. 3, Apr. 2018, Art. no. 5200306.
[25] N. Bianchi and H. Mahmoud, "An analytical approach to design the PM in PMAREL motors robust toward the demagnetization," *IEEE Trans. Energy Convers.*, vol. 31, no. 2, pp. 800–809, Jun. 2016.
[26] M. Z. Islam, A. Arafat, S. S. R. Bonthu, and S. Choi, "Design of a robust five-phase ferrite-assisted synchronous reluctance motor with low demagnetization and mechanical deformation," *IEEE Trans. Energy Convers.*, vol. 34, no. 2, pp. 722–730, Jun. 2019.
[27] B. Wang, J. Hu, W. Hua, and Z. Wang, "Fault operation analysis of a ripplee-redundant three-phase PMA-SynRM for EV application," *IEEE Trans. Transp. Electrific.*, vol. 7, no. 1, pp. 183–192, Mar. 2021.
[28] B. Wang, J. Wang, A. Griffo, and Y. Shi, "Investigation into fault-tolerant capability of a triple redundant PMA SynRM drive," *IEEE Trans. Power Electron.*, vol. 34, no. 2, pp. 1611–1621, Feb. 2019.
[29] B. Wang, J. Wang, and A. Griffo, "Stator turn fault modeling for a triple redundant 3×3-phase PMA SynRM," *IEEE Trans. Ind. Electron.*, vol. 66, no. 6, pp. 4220–4242, Jun. 2019.
[30] J.-K. Park, C. Babetto, G. Berardi, J. Hur, and N. Bianchi, "Comparison of fault characteristics according to winding configurations for dual three-phase synchronous reluctance motor," *IEEE Trans. Ind. Appl.*, vol. 57, no. 3, pp. 2398–2406, May/Jun. 2021.
[31] N. Bianchi, J. Park, A. Tortella, and R. Zavagnin, "Experimental tests of dual three-phase synchronous reluctance motor under half-control mode," *IEEE Trans. Ind. Appl.*, vol. 57, no. 6, pp. 5887–5893, Nov./Dec. 2021.
[32] A. Griffo, R. Wrobel, P. H. Mellor, and J. M. Yon, "Design and characterization of a three-phase brushless exciter for aircraft starter/generator," *IEEE Trans. Ind. Appl.*, vol. 49, no. 5, pp. 2106–2115, Sep./Oct. 2013.
[33] R. Wrobel *et al.*, "Design study of a three-phase brushless exciter for aircraft starter/generator," in *Proc. IEEE Energy Convers. Congr. Expo.*, 2011, pp. 3998–4004.
[34] N. Bianchi, S. Bolognani, and M. D. Pre, "Strategies for the fault-tolerant current control of a five-phase permanent-magnet motor," *IEEE Trans. Ind. Appl.*, vol. 43, no. 4, pp. 960–970, Jul./Aug. 2007.
[35] B. C. Mecrow, A. G. Jack, J. A. Haylock, and J. Coles, "Fault-tolerant permanent magnet machine drives," *IEE Proc. Electric Power Appl.*, vol. 143, no. 6, pp. 437–442, 1996.
[36] J. A. Haylock *et al.*, "Operation of a fault tolerant PM drive for an aerospace fuel pump application," *IEE Proc. - Electric Power Appl.*, vol. 145, no. 5, pp. 441–448, 1998.
[37] K. W. Klontz, T. J. E. Miller, M. I. McGilp, H. Karmaker, and P. Zhong, "Short-Circuit analysis of permanent-magnet generators," *IEEE Trans. Ind. Appl.*, vol. 47, no. 4, pp. 1670–1680, Jul./Aug. 2011.
[38] J. Xu, B. Zhang, X. Kuang, H. Guo, and S. Guo, "Influence analysis of slot parameters and high torque density optimization for dual redundant permanent magnet motor in aerospace application," *IET Electr. Power. Appl.*, vol. 14, no. 7, pp. 1263–1273, 2020.

Hong Guo (Senior Member IEEE) received the B.S., M.S., and Ph.D. degrees in electrical engineering from Harbin Institute of Technology, Heilongjiang, China, in 1988, 1991 and 1994, respectively.

He is currently a Professor with the School of Automation Science and Electrical Engineering, Beihang University, Beijing, China. His research interests include design and control of permanent magnet motor, robust design theory and method of electrical machine, and design theory and method of electrical machine with high reliability.

Xu He received the B.S. degree in electrical engineering in 2015 from the School of Automation Science and Electrical Engineering, Beihang University, Beijing, China, where he is currently working toward the Ph.D. degree in electrical engineering with the School of Automation Science and Electrical Engineering.

His research interests include design of high-speed high-power aircraft starter-generator system and permanent magnet assisted synchronous reluctance starter-generator.

Jinquan Xu (Senior Member IEEE) received the B.S. and Ph.D. degrees in electrical engineering from the School of Automation Science and Electrical Engineering, Beihang University, Beijing, China, in 2009 and 2015, respectively.

From 2012 to 2013, he was a visiting scholar with George W. Woodruff School of Mechanical Engineering, Georgia Institute of Technology, Atlanta, USA. He is currently an Associate Professor with the School of Automation Science and Electrical Engineering, Beihang University, Beijing, China. His research interests include fault tolerant permanent magnet motor systems, position sensorless control of fault tolerant motors, fault diagnosis, and robust control.

Wei Tian received the M.S. degree in electrical engineering from the Guangdong University of Technology, Guangzhou, China, in 2012, and the Ph.D. degree in electrical engineering from the School of Automation Science and Electrical Engineering, Beihang University, Beijing, China, in 2019.

He is currently with the School of Electrical Information Engineering, Jiangsu University, Zhenjiang, China. His main research interests include the design theory and method of electrical machine with high power density and high efficiency applied in aircraft and electric vehicles.

Gaoyang Sun received the B.S. degree in electrical engineering and its automation from Henan University of Technology, Zhengzhou, China, in 2015, and the M.S. degree in electrical engineering from Beijing Jiaotong University, Beijing, China, in 2018. He is currently working toward the Ph.D. degree in electrical engineering with Beihang University, Beijing, China.

His research interests include control of aircraft starter/generator system and design of aircraft power electronic converter.

Laicai Ju received the M.S. degree in electrical engineering from the School of Automation Science and Electrical Engineering, Beihang University, Beijing, China, in 2015.

He is currently with the Beijing Shuguang Electric Limited Liability Company, Beijing, China. His research interest includes design of aircraft electrical machine.

Dehong Li received the B.S. degree in electrical engineering from Nanjing University of Aeronautics and Astronautics, Nanjing, Jiangsu, China, in 1992. He is currently with the China Helicopter Design and Research Institute, Tianjin, China. His research interest includes design of aircraft electrical machine.